Thaw-driven mass wasting couples slopes with downstream systems and effects propagate through Arctic drainage networks.

Steven V. Kokelj[1], Justin Kokoszka[1,2], Jurjen van der Sluijs[3], Ashley C.A. Rudy[1], Jon Tunnicliffe[4], Sarah Shakil[5], Suzanne E. Tank[5], Scott Zolkos[5,6]

[1]Northwest Territories Geological Survey, Yellowknife, NT, X1A 2L9, Canada

[2]Wilfrid Laurier University, Yellowknife, NT, X1A 2L9, Canada

[3]Northwest Territories Centre for Geomatics, Yellowknife, NT, X1A 2L9, Canada

[4]School of Environment, University of Auckland, Auckland, NZ

[5]Department of Biological Sciences, University of Alberta, Edmonton, AB, T6G 2E3, Canada

[6]Woodwell Climate Research Centre, Falmouth, MA, 02540, USA

Correspondence to: Steven V. Kokelj (steve_kokelj@gov.nt.ca)

Abstract.

The intensification of thaw-driven mass wasting is transforming glacially-conditioned permafrost terrain, coupling slopes with aquatic systems and triggering a cascade of downstream effects. Within the context of recent, rapidly evolving climate controls on the geomorphology of permafrost terrain we: A) quantify three-dimensional slump enlargement and describe the processes and thresholds coupling slopes to downstream systems; B) investigate catchment-scale patterns of slope thermokarst impacts and the geomorphic implications; and C) map the propagation of effects through hydrological networks draining continuous permafrost of northwestern Canada. Power-law relationships between thaw-slump area and volume (R^2 = 0.90), and thickness of permafrost thawed (R^2 = 0.63), combined with the multi-decadal (1986-2018) increase in areal extent of thaw-slump disturbance show a two-orders of magnitude increase in catchment-scale geomorphic activity and the coupling of slope and hydrological systems. Predominant effects are to first- and second-order streams where sediment delivery, often indicated by formation of recent debris tongue deposits, commonly exceeds the transport capacity of headwater streams by orders of magnitude indicating centennial to millennial-scale perturbation of downstream systems. Assessment of hydrological networks indicates thaw-driven mass wasting directly affects over 6,760 km of stream segments, 890 km of coastline and 1,370 lakes in the 994,860 km^2 study area. Downstream propagation of slope thermokarst indicates a potential increase in the number of affected lakes by at least a factor of 4 (n >5,600), impacted stream length by a factor of 7 (>48,000 km) and defines several major impact zones to lakes, deltas and coastal areas. Prince of Wales Strait is the receiving marine environment for greatly increased sediment and geochemical fluxes from numerous slump impacted hydrological networks draining Banks and Victoria Islands. Peel and Mackenzie Rivers are globally significant conveyors of the slope thermokarst cascade delivering effects to North America's largest Arctic delta and the Beaufort Sea. Climate-driven erosion of ice-rich slopes in permafrost-preserved glaciated terrain has triggered a time-transient cascade of downstream effects that signal the renewal of post-glacial landscape evolution. Glacial legacy, ground-ice conditions and the patterns of continental drainage dictate that terrestrial, freshwater, coastal, and marine environments of western Arctic Canada will be an interconnected hotspot of thaw-driven change through the coming millennia.

1 Introduction

Climate-induced permafrost thaw will drive the geomorphic evolution of circumpolar ice-rich landscapes (Kokelj and Jorgenson, 2013), and terrestrial, freshwater and coastal ecosystems (Vonk et al., 2019). Thawing of ice-rich, glacially-conditioned permafrost terrain (Kokelj et al., 2017a) is rapidly mobilizing vast stores of previously frozen materials, reconfiguring slopes and impacting downstream environments (Fig. 1) (Balser et al., 2014; Rudy et al., 2017a; Tank et al., 2020). These and other similar results highlight the need to quantify slope thermokarst intensification in a robust physical framework, better understand the rapidly evolving linkages between thawing slopes and downstream environments, and predict the propagation of effects across watershed scales.

The nature of permafrost thaw and downstream consequences will define trajectories of environmental change in Arctic terrestrial and aquatic systems. Study of thawing slopes and shorelines (Lacelle et al., 2010; Ramage et al., 2017; West and Plug, 2008), and characterization of permafrost physical and geochemical properties (Lacelle et al., 2019), informs the projection of downstream cumulative-effects and implications for carbon and contaminant mobilization (Littlefair et al., 2017; Ramage et al., 2018; St. Pierre et al., 2018; Tank et al., 2020). Recent, rapid increases in the areal extent of upland thermokarst (Lewkowicz and Way, 2019; Segal et al., 2016a; Ward-Jones et al., 2019), and shifts in hydrological, sedimentary and geochemical regimes (Abbott et al., 2015; Kokelj et al., 2013; Littlefair et al., 2017; Rudy et al. 2017a) can be linked with significant aquatic ecosystem impacts (Chin et al., 2016; Houben et al., 2016; Levenstein et al., 2018; Thienpont et al., 2013). The processes and feedbacks driving the evolution of thawing slopes (Kokelj et al., 2015; Zwieback et al., 2018) have received less attention. Thaw-driven landslide effects on permafrost catchments have been investigated through nested watershed studies (Beel et al., 2018; Bowden et al., 2008; Shakil et al., 2020a; Zolkos et al., 2020), and the cascade of effects have been inferred through geochemical trend analyses of large Arctic rivers (Tank et al., 2016; Zolkos et al., 2018). The broad-scale distribution of slope thermokarst determined through empirical (Kokelj et al., 2017a), remote sensing (Brooker et al., 2014; Nitze et al., 2018), GIS mapping (Olefeldt et al., 2016) and modelling approaches (Rudy et al., 2017b) have typically not been designed to elucidate physical processes, downstream connectivity and attendant effects. Despite the growing geomorphic and geochemical influence of thaw-driven mass wasting on terrestrial, aquatic and marine systems (Vonk et al., 2019), and the potential for rapid carbon release (Turetsky et al., 2020), fundamental knowledge gaps persist in our understanding of climate-driven amplification of slope thermokarst, the evolution of downstream linkages and the cascade of consequences.

Retrogressive thaw-slumps, complex thaw-flow slides, and shallow and deep translational failures are amongst the most dynamic forms of slope thermokarst (Alysworth, 2000; Kokelj et al., 2015; Rudy et al., 2017b). Anticipating the cumulative effects of thaw-driven mass wasting on permafrost landscapes and downstream environments requires a better knowledge of processes and the evolution of connectivity across a range of spatial scales. First, exploring the implications of thaw-driven mass wasting requires determining the relationships between disturbance area, volume, and thickness of permafrost thawed

so that changes in landslide count or areal extent (Lantz and Kokelj, 2008; Lewkowicz and Way, 2019; Ward-Jones et al., 2019) can be considered in a more robust physical framework (van der Sluijs et al., 2018). To advance understanding of processes and feedbacks driving the evolution of slope thermokarst and hillslope-channel coupling, conventional satellite- and airborne-derived planform terrain assessments should be quantified with high-resolution 3D survey techniques. Secondly, analysing thermokarst mass-wasting effects within a hydrological network context is required to understand slope-to-stream linkages and downstream connectivity (Wohl et al., 2019), and to provide a platform for description and modelling of watershed effects. Finally, considering the distribution of thermokarst mass-wasting processes and trajectories of change within an appropriate theoretical or geomorphic context (Ballantyne, 2002) will support the explanation of spatial patterns, rates and magnitudes of geomorphic change (Kokelj et al., 2017a), and geochemical effects (Lacelle et al., 2019; Tank et al., 2020), and contextualize conceptual and physically-based models (Turetsky et al., 2020).

The aims of this study are to better understand (A) the geomorphic changes that result from thaw-driven mass wasting and the evolution of slope to stream coupling, (B) the spatial distribution of catchment effects, and (C) their propagation across watershed scales. Here we present a suite of spatially nested case-studies bounded by Arctic drainage from continuous permafrost of northwestern Canada (Fig. 1). This 10^6 km^2 study region contains a wide range of climate and permafrost temperature regimes (Smith et al., 2010), ground ice conditions (O'Neill et al., 2019), biophysical gradients (Lantz et al., 2010), and geological environments, including unglaciated and glaciated terrain (Dyke and Prest, 1987; Dyke et al., 2003). The latter is of central relevance to study design, in particular where permafrost has maintained ice-marginal moraine, glaciolacustrine, glaciofluvial and glaciomarine deposits in a quasi-stable state, preserving relict ground ice (Lakeman and England, 2012; Mackay, 1971; Murton et al., 2005; Pollard, 2000) and constraining slope evolution through a cooling Holocene climate (Porter et al., 2019). Today, these environments host large areas affected by intense thaw-driven geomorphic change (Fig. 1) where landslides, predominantly in the form of retrogressive thaw slumps, or retrogressive thaw-flow slides, are mobilizing slope materials, transforming landscapes (Kokelj et al., 2015), and triggering an array of downstream effects (Chipman et al., 2016; Rudy et al., 2017a; Zolkos et al., 2018). The fine-scale investigations in this research focused on retrogressive thaw slumping because it is a primary mode of thaw-driven slope failure in the study region (Segal et al., 2016a), and often a modifier of slopes affected by other landslides types. Broad-scale mapping to address goal (C) considered multiple slope failure modes (thaw slumps, shallow and deep translational slides), so we utilized more inclusive terminology such as slope thermokarst, thaw-driven landslides or mass wasting when discussing these results.

To quantify the enlargement of retrogressive thaw slumps, assess allometric relationships (i.e. area and volume) (cf. Bull, 1964), and to explore thresholds that govern slope-to-stream connectivity (Goal A) we analysed fine-scale topographic data derived from LiDAR for a large population of thaw slumps from across the Peel Plateau (Kokelj et al., 2017b), and Anderson Plain and Tuktoyaktuk Coastlands areas (Rampton, 1988), and from repeat Unmanned Aerial Vehicle (UAV) terrain surveys of individual disturbances on the Peel Plateau (Fig. 1, Table S1). To investigate thermokarst mass-wasting

effects on catchments (Goal B), we combined thaw-slump mapping with empirical models to estimate disturbance volume, to visualize the patterns and intensity of impacts across a fluvial network, and to derive first-order estimates of slope denudation for a medium-sized catchment (Willow River, 10^3 km^2) in the Mackenzie Delta region (Fig. 1, Table S1). Detailed investigations of the distribution of thermokarst mass wasting within a fluvial network were extended to a range of catchments for the northern Peel Plateau (3,520 km^2) and southeastern Banks Island (1,220 km^2), and patterns of fluvial-geomorphic effects were explored by contrasting stream sediment fluxes across catchment scale and disturbance status. To assess the potential propagation of watershed-scale slope thermokarst effects (10^4 to 10^5 km^2) (Goal C), disturbance distribution was analysed within a Strahler-order framework for the Banks Island, Amundson Gulf, Peel River and Keele/Redstone watersheds (Fig. 1, Table S1). Finally, thaw-driven mass wasting effects on stream, lake and coastal environments were integrated through a flow accumulation analysis to map the potential cascade of effects through hydrological networks of northwestern Canada (Fig. 1). Through this multi-scale study we link the intensification of thaw-driven slope processes with the coupling of downstream systems and we map the propagation of effects through hydrological networks, showing the interconnected nature of slope thermokarst hotspots, and the patterns of emerging sedimentary and geochemical regimes that will define major Arctic change through the coming millennia.

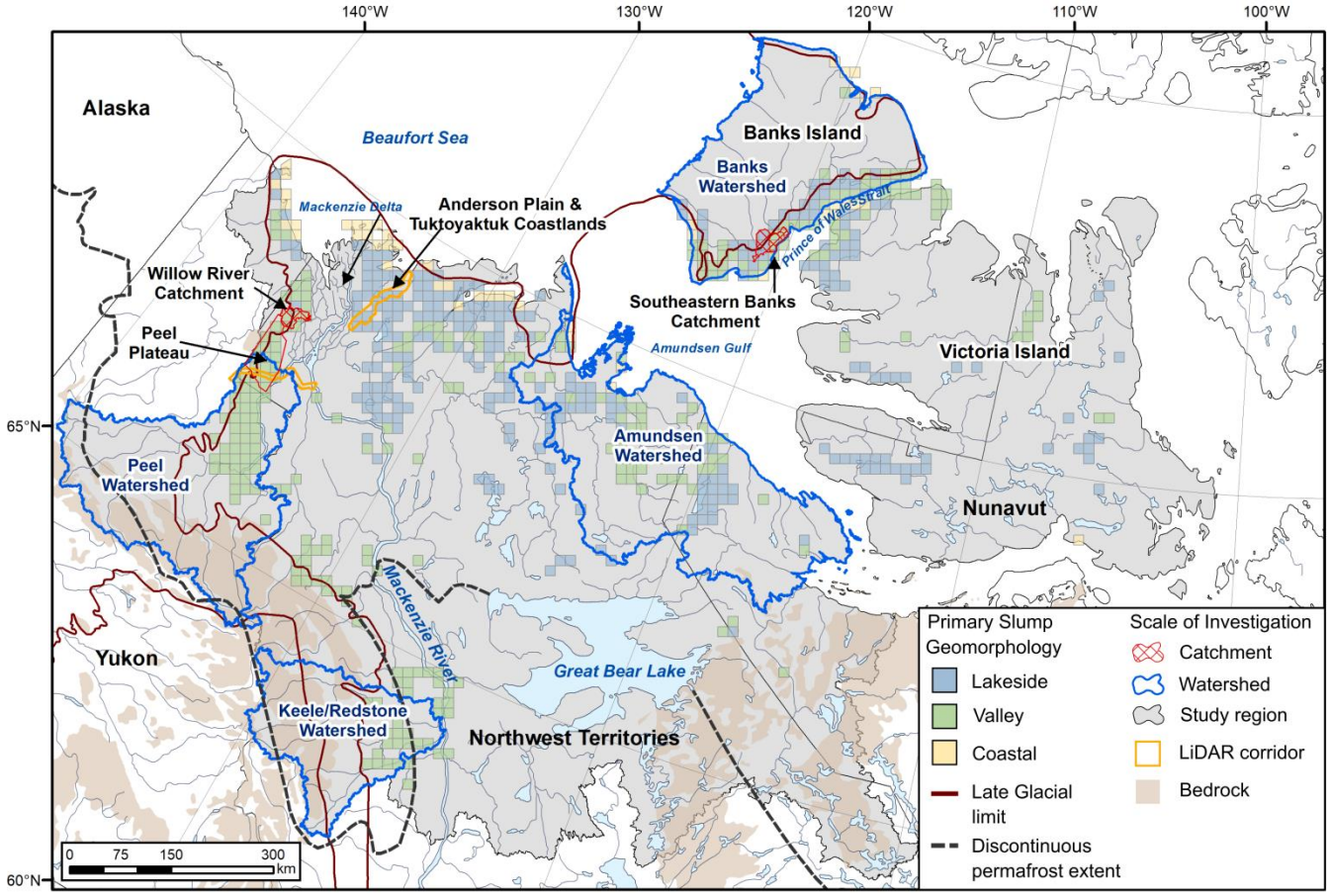

Figure.1. Study region map showing the distribution and dominant geomorphic environments affected by thaw-driven mass wasting, and the locations and scales of investigation constrained by the 994,860 km^2 area of Arctic drainage from continuous permafrost of northwestern Canada. Fine-scale thaw slump mapping utilizing high resolution UAV and LiDAR terrain models is indicated by the orange corridors (Peel Plateau and Tuktoyaktuk Coastlands and Anderson Plain); small to medium scale catchments including Willow River, Peel Plateau and southeastern Banks Island areas are indicated by red polygons; major watersheds are outlined in blue and Arctic drainage from continuous permafrost is shaded in grey. The disturbance data on the map are adapted from Segal et al., 2016b and Kokelj et al., 2017a. Late glacial limit is from Dyke and Prest, 1987, bedrock geology is from Fulton, 1995 and the permafrost boundary is from Brown et al., 1997. Base map is from ESRI ArcGIS Online.

2 Study area and methods

2.1 Study Area

This study area defined as Arctic drainage from continuous permafrost of northwestern Canada comprises an area of 994,860 km^2, and it is characterized by diverse permafrost, geological, climate and ecosystem conditions (Fig. 1). The Mackenzie and Peel River systems drain the south central and western parts of the study area. Several small hydrological systems characterize the Yukon Coastal plain, whereas medium to large northward flowing rivers drain tundra of the interior platform and shield terrain northeast of the Mackenzie Basin. An abundance of small to medium sized streams comprises tundra watersheds of Banks and Victoria Islands. The study area is characterized by warm permafrost in the southern and western regions where mean annual temperatures at the top of permafrost (TTOP) in undisturbed forested and alpine tundra terrain range from above -1°C to about -3°C (Smith et al., 2010; O'Neill et al., 2015), a transition to low Arctic tundra where permafrost is typically greater than 100 m in thickness with mean annual TTOP below -4°C (Kokelj et al., 2017c), and Arctic tundra of Banks and Victoria Islands where frozen ground is hundreds of metres thick and mean annual TTOP is typically below -10°C (Smith et al., 2010). Abundant ice-rich terrain in the region is indicated by the widespread occurrence of segregated, wedge, and relict ground ice (O'Neill et al., 2019 and references within). The distribution and abundance of these main ground-ice types are associated with the legacy of glaciation, distribution of fine-grained, frost-susceptible sediments and a cold Holocene climate. The spatial distribution of retrogressive thaw slumps confirms the abundance of ice-rich terrain and thaw sensitive slopes, and the broad-scale association with ice-marginal, permafrost preserved glacigenic terrain (Fig. 1) (Kokelj et al., 2017a). The unglaciated western margins of the study region are mountainous and permafrost is generally ice-poor. Numerous high energy streams and rivers draining the Cordillera have incised unconsolidated, ice-rich glacial deposits along their course to the Mackenzie or Peel Rivers. These thick deposits of fine-grained tills and other glacigenic materials, derived primarily from sedimentary bedrock, define the western margins of the Laurentide glacial limits and contrast with the eastern part of the study region characterized by shield bedrock veneered by patches of glacial materials derived from Precambrian rock (Dyke and Prest, 1987). The predominant form of slope thermokarst mass-wasting across the region is retrogressive thaw slumps (Kokelj et al., 2017a), with shallow and deep-seated landslides having local importance that increases southward, particularly in areas of greater relief (Aylsworth et al., 2000). To examine the processes driving intensification of thaw-driven mass wasting and the patterns of effects across hydrological networks we applied multiple methods involving field study and mapping at slope, catchment, and watershed scales described in the following sections and summarized in Table S1.

2.2 Fine-scale topographic data to explore hillslope-channel coupling

To describe processes of thaw slump development and slope-to-stream connectivity, terrain surveys by airborne LiDAR from fixed-wing aircraft and structure from motion (SfM) photogrammetry from UAV were used to derive a sequence of

Digital Terrain Models (DTMs) (van der Sluijs et al., 2018) covering an 8-year span from 2011 to 2018. These surveys comprised a series of DTMs enabling total and annual volumes of material displaced by thaw-driven mass wasting to be estimated by: 1) calculating differenced DTMs (DOD); 2) determining uncertainties and masking DODs based on minimum levels of change detection thresholds; and 3) summarizing the values for the scar-zone (erosion) and debris tongue (deposition). Full data acquisition and processing methods are provided in van der Sluijs et al (2018). Survey metadata are provided in Table S2.

Overlapping UAV photos were acquired from a size continuum of slumps on the Peel Plateau (Fig. 1) between 2015 and 2018, along with ground control data acquired through differential Global Navigation Satellite System (GNSS) surveys. Aerial photo datasets were processed into georeferenced colour orthomosaics and point clouds using SfM software packages (Smith et al., 2016). Noise-filtered and ground-classified point clouds were rasterised in 0.5-m spatial resolution bare-earth DTMs and resampled bilinearly to 1 m spatial resolution for spatial consistency with LiDAR models. The LiDAR data with an average point density of 1.7 m^{-2} was collected on 25-28 August 2011 by vendor McElhanney Consulting Services Ltd. (Vancouver, BC, Canada) along two study corridors (Fig. 1). The first is a 162 km long, 6-9 km wide portion of the Dempster Highway across the Peel Plateau comprising an area of 1,032 km^2 (O'Neill et al., 2015; Kokelj et al., 2017b). The second corridor is a 9-19 km wide and 139 km long area 1,478 km^2, comprising the Inuvik-to-Tuktoyaktuk Highway corridor which crosses the Anderson Plain and Tuktoyaktuk Coastlands (Rampton, 1988). Following initial processing by the vendor, a baseline 1-m LiDAR DTM was created in ESRI ArcGIS 10.4.1 ("LAS Dataset to Raster" tool) using mean ground point elevations and Delaunay triangulation with linear interpolation to fill data voids. Vertical datum differences between the LiDAR and UAV surveys were corrected to ensure data compatibility.

To explore the associations between thaw slump enlargement and slope-to-stream coupling, we quantified the volumes of slump erosional concavities and debris tongue deposits for a size-age continuum exemplified in five disturbances in the Peel Plateau region where DTM data was derived from 2018 UAV surveys (Table S2). Notably, geomorphic activity at one of the thaw slumps (CB) had accelerated significantly throughout the monitoring record (2011-2018). The 2011 LiDAR DTM provided a topographic baseline that could be used to reconstruct pre-disturbance terrain surfaces so that volumetric changes associated with thaw-driven subsidence and slope erosion, and downstream deposition could be estimated. The pre-disturbance surfaces were manually reconstructed using LiDAR-derived 2-m contours aided by historical aerial photographs, and circa 1970 Canadian Digital Elevation Model (CDEM) (Natural Resources Canada, 2015), following van der Sluijs et al. (2018). Pre-disturbance valley morphology required valley-bottom elevations to be constrained, so undisturbed stream elevations were sampled at 10 m intervals up to 200 m above and below debris tongue deposits. Fitted polynomial curves were used to model pre-disturbance valley bottoms, constraining contour line reconstructions, which were interpolated to a 1-m DTM using the ArcGIS 10.4.1 "Topo-to-Raster" tool. Total scar zone and debris tongue volumes were estimated, and DODs provided a volumetric estimate of the year to year changes.

2.3 Regional Scale Data Acquisition and Processing

To explore relationships between planform thaw slump scar area and volume we digitized scar areas, and estimated the volume and depth of the disturbance concavities for a subsample of 71 thaw slumps from the 2011 LiDAR corridors described in Sect. 2.2 and shown on Figure 1. Features were digitized by J. van der Sluijs and reviewed for accuracy and consistency by SV Kokelj (Table S1). Utilizing LiDAR hill-shaded DTMs and optical airborne imagery (2011-2012), all active or recently-active scar and debris tongue areas determined by a distinct scarp and bare or sparsely vegetated scar area were digitized at a 1:2,000 scale. Each polygon defined either a scar zone where the debris tongue was indistinguishable or a scar-only area where a debris tongue could be identified as a geomorphic feature distinct from the active scar zone. Slumps were designated as being associated with fluvial, lacustrine or coastal systems, with an assigned integer to indicate the downstream connectivity, where "0" is no connection with the downstream environment; "1" is connection between the bare scar area and downstream environment, and "2" indicates evidence of downstream deposition, which is expressed as a debris tongue in a valley bottom, or a sediment lobe protruding into an adjacent lake or coastline.

For developing regional-scale slump DTMs and DODs we followed general procedures described in Sect. 2.2, with some adaptations to streamline processing of a large sample population. Firstly, only "classic" cuspate or bowl shaped thaw slump forms were assessed: more complex elongated and polycyclic features, common along shorelines, introduced greater uncertainty in the process of automated pre-disturbance terrain reconstruction. Several parameter adjustments in ArcGIS LAS Dataset to Raster tool were implemented to minimize vegetation influences. Rather than linearly triangulating mean elevation of ground-classified points, minimums were binned into a 1-m grid to better represent ground elevation in (re-)vegetated terrain (Gould et al., 2013; Meng et al., 2010). Reconstructing pre-disturbance slump topography was automated by removing all points in the slump scar and interpolating the pre-disturbance surface with points adjacent to the scar. Natural neighbour void-filling interpolation was applied as a balance between accuracy and shape reliability across a range of natural environments (Bater and Coops 2009; Boreggio et al., 2018). The 2011 LiDAR and derived pre-disturbance DTMs were differenced into a DOD, and results were summarized with ArcGIS Zonal Statistics.

2.4 Catchment scale mapping and analyses of sediment flux

To examine the patterns of thaw-slump occurrence within a drainage network, slope to stream connectivity and change through time, we investigated the 806 km^2 Willow River catchment on Peel Plateau because it straddles the late Wisconsinan glacial limit and much of the fluvially-incised basin is intensely affected by thaw slumping (Fig. 1) (Lacelle et al., 2010). To examine temporal change we created digitized inventories of active thaw slumps from the Willow River catchment utilizing cloud-free Landsat imagery from 1986, 2002 and 2018 (Table S1) (Rudy and Kokelj, 2020). To further explore catchment-scale patterns of slope disturbances over multiple watersheds in different regions, and potential changes in these patterns

through time we used 2016-2017 Sentinel-2 imagery to re-assess the 2005-2010 slump mapping determined using SPOT 4/5 satellite imagery (Segal et al., 2016c, d) for a 3,520 km^2 area of the northern Peel Plateau and 1,220 km^2 of southeastern Banks Island (Fig. 1) (Rudy et al., 2020). To assess the distribution of thaw slumps within a catchment framework, we used CDEM, and applied Tau-DEM (v.5.3) Fill, D8, and Flow Accumulation algorithms (http://hydrology.usu.edu/taudem/) (Tarboton, 1997) to trace the drainage networks and determine the upstream contributing area for each thaw slump.

Sediment fluxes for Peel Plateau streams draining glaciated and unglaciated terrain were calculated to assess effects of catchment size and thermokarst disturbance (Shakil et al., 2020b). Instantaneous total suspended sediment (TSS) fluxes (mg km^{-2} s^{-1}) were compiled from sampling during the summer flow period (July – September) for 2010 and 2015-2017. Sampling procedures and catchment delineations are elaborated in Chin et al., 2016 and Shakil et al., 2020a. Historical TSS yields also constrained to July 1st – September 14th were obtained for the Peel River at Fort McPherson (Water Survey of Canada, station 10MC002), by pairing TSS spot sampling with discharge and normalizing to a 70,506 km^2 watershed area.

2.5 The influence of thaw-driven mass wasting on drainage from continuous permafrost of northwestern Canada

Here we summarize methods to identify individual segments of the hydrological network affected by active thaw-driven mass wasting and the framework to map the propagation pathways of effects through watersheds for Arctic drainage from continuous permafrost of northwestern Canada (Fig. 1). Geoprocessing steps are in Supplementary methods 1-3 and the mapping procedure and raw data are in Kokoszka and Kokelj (2020). In summary, we used georeferenced, 10m resolution SPOT 4/5 (2005-2010) (NWT Centre for Geomatics, 2013) and Sentinel-2 (2016-2017) orthomosaics to identify hydrological segments affected by mass wasting features for individual stream network, lake, and coastline segments from the 1:50,000 National Hydro Network (NHN) dataset (Natural Resources Canada, 2016) using ArcMap 10.6. The Arctic drainage area contains 68 NHN Work Units (subcatchments). The NHN Primary Directed Network Linear Flow (PDNLF) Shapefiles include primary (main route) stream segments and polylines through lakes, and the NHN Waterbody and Littoral Shapefiles represent lakes and coastlines, respectively. This dataset was combined to define the entire NHN hydrological network for the 994,860 km^2 drainage area (Fig. 1).

A 7.5x7.5 km grid system guided the systematic inventory of thermokarst affected hydrological segments in each of the 68 NHN work units (Kokoszka and Kokelj, 2020). NHN hydrological features were designated as ‘directly affected’ where one or more active slope thermokarst disturbances were in contact with, or exhibited clear drainage towards the hydrological feature. PDNLF features directly influenced by thaw-driven mass wasting were assigned a numeric value of '1'. To enable propagation of effects from lakes, PDNLF features at the lake outflow within directly affected lakes were also assigned a numeric value '1'. Unaffected PDNLF features were assigned a numeric value '0' to indicate no thermokarst effect. All mapping was reviewed for accuracy and consistency (Kokoszka and Kokelj, 2020).

The potential for downstream propagation of slope thermokarst effects was determined by generating a network for each of the 68 Work Units using RivEX 10.25 (Hornby, 2017). A river network was constructed for each PDNLF dataset based on the topology of the original NHN data, where the digitized direction corresponded with flow direction. PDNLF features directly affected by one or more slope-thermokarst features were assigned a value of '1' as indicated above. The 'Accumulate Attribute Tool' in RivEX 10.25 was used to sum the number of all upstream slope thermokarst affected segments and tabulated for each Work Unit. One 800 km^2 catchment (Willow River, see Fig. 1) representing a subset of the total stream network was subjected to additional analysis since detailed thaw-slump mapping (Rudy et al., 2020) was available. The total area of mapped thaw slumps and slides for each hydrological segment was summed and accumulated downstream to portray catchment-scale variation in the intensity of disturbance effects (Supplementary Methods 1).

For the broad and fine-scale analyses the accumulated count of impacted stream segments was used to identify the longitudinal trace of mass wasting effects within each Work Unit (Supplementary Methods 2). Stream features with an accumulation value > 0 represented the potential propagation pathway of effects through the network. Propagation of effects across watershed scales involved transferring accumulation values from upstream to downstream Work Units. Hydrological features that were influenced by the downstream propagation of slope thermokarst effects were identified as indirectly affected PDNLF features with an accumulation value > 0 and a numeric value of 0. PDNLF features contained within lakes with an accumulation value > 0 indicated indirectly affected lakes, although these lakes could also be attributed as directly affected if the shoreline hosted slope thermokarst features. Coastal segments adjacent to accumulated PDNLF features where streams discharge to the ocean were identified as indirectly affected coastline. After all Work Units were processed, the data were merged to produce a downstream trace with upstream accumulation values for the entire 994,860 km^2 drainage area.

To summarize information on the distribution of watershed effects, Strahler Order was computed (Supplementary Methods 3) for the 4 major watershed areas of Banks Island (70,794 km^2), Amundsen Gulf (90,288 km^2), Peel River (76,506 km^2), and Keele/Redstone (39,957 km^2) (Fig. 1). For each major watershed, the respective Work Unit and PDNLF Shapefiles were merged and the 'Strahler Order Tool' in RivEx 10.25 was used to compute Strahler Order for each PDNLF polyline. For each sub-basin, directly and indirectly affected streams and lakes were summarized by Strahler Order.

We summarized the total length of thermokarst-affected stream networks and the coastal margins, as well as the total number of thermokarst affected lakes, including lakes influenced by the downstream propagation of disturbance effects. Mid-points of the directly affected stream, lake and coastal segments were synthesized in ArcGIS to create a kernel density map. The routing of thermokarst effects was portrayed through the downstream trace and accumulation values at the coastline to provide a relative estimate of the magnitude of upstream effects. This current method does not account for variation in transport gradients, catchment sinks, nor intensity of each disturbance, and therefore represents a semi-quantitative, time-transient snapshot of thaw-driven mass wasting effects on drainage from continuous permafrost of northwestern Canada.

2.6 Statistical analyses

The software package SPSS Statistics 21 (IBM) was used for data exploration, deriving summary statistics, testing inferential qualities, and regression analyses for all LiDAR and UAV derived datasets presented in this study. All summary statistics are provided in tabular format in the body of the manuscript or Supplementary materials. Thaw-slump area, volume and maximum depth of disturbance concavity did not meet assumptions of normality and were logarithmically transformed prior to performing a t-test to assess differences in slump size metrics between physiographic regions, and a one-way analysis of variance and a Tukey's HSD post-hoc test to assess differences across categories describing downstream connectivity. Regression analyses between thaw-slump area and disturbance volume, and thaw-slump area and maximum concavity depth were also performed on the logarithmically transformed datasets. Regression diagnostics included testing the normality of residuals, and Cook's distance to test for the presence of unduly influential points. Additional statistical analyses assessing thaw-driven landslides in the Willow River catchment and potential changes through time were performed in RStudio (Version 1.1.463) using the "stats" and "FSA" packages (R Core Team, 2017). In this case study, non-parametric statistical testing (Kruskall-Wallis and Dunn's post-hoc tests) was implemented to assess potential differences in slump size indices between 3 different time periods.

3 Results

Here we document: (A) the rapid evolution of thaw-driven mass wasting and slope-to-stream coupling, (B) the spatial patterns of thermokarst effects within catchments, and (C) their propagation through hydrological networks and across watershed scales. The first three subsections focus on slope-scale processes with emphasis on the thresholds that have transformed connectivity between thaw-driven mass wasting and downstream systems (3.1, 3.2), and the scaling of thaw-slump dimensions associated with areal enlargement (3.3). The fourth and fifth subsections (3.4, 3.5) focus on quantifying the changing patterns and magnitudes of thermokarst and the potential downstream effects within hydrological networks up to the medium catchment (10^4 km^2) scale. The final subsection (3.6) provides flow accumulation analysis results that explore patterns and project the routing of thermokarst mass wasting effects through Arctic drainage networks from continuous permafrost of northwestern Canada.

3.1 Thaw slump intensification transforms slope-to-stream connectivity

To investigate geomorphic change associated with thaw slump enlargement and the evolution of linkages between thawing slopes and downslope environments we used UAV-derived elevation data from 2018 to quantify thaw slump and debris tongue volumes for a size and age disturbance continuum on the Peel Plateau (Tables 1, S2; Figs. 2, S1). The smallest slump (slump D1) which was about a decade old, had an area of 2.8 x 10^3 m^2, a displaced volume of 4.6 x 10^3 m^3, and no debris tongue accumulation (Table 1; Fig. 2a, g). The second-largest feature (slump CB), which initiated around 2002-2004 had recently accelerated growth, displacing 1.36 x 10^5 m^3 and forming a debris tongue comprising 20% of the scar volume (Fig.

2b, g; Table 1). The geomorphic acceleration of slump CB occurred through our monitoring period (Fig. 3). Over 2 decades, two larger slumps, FM3 and Husky, displaced 5.0 x 10^5 m^3 and 6.9 x 10^5 m^3 of material producing debris tongues of 1.5 x 10^5 m^3 and 3.7 x 10^5 m^3, respectively (Table 1). The valley-fills exceed 15 m thickness and approach 1000 m length (Fig. 2g), comprising about 30% (FM3) and 50% (Husky) of the estimated scar cavity volumes (Table 1). At Husky slump, the debris tongue raised the base-level of the trunk stream, elevating and laterally displacing the stream channel against the side of the valley, causing lateral erosion and secondary slump initiation (Fig. 2c). Growth of the Husky slump led to the breaching and rapid lake drainage in 2015, which flushed scar colluvium down valley (Video S1).

Table 1. Scar and debris tongue areas and volumes (sediment erosion and thaw subsidence vs. deposition) and debris tongue age for a ~~slump-size~~ continuum from September 2018 field observations. Terrain models and delineations of these disturbances are shown in Figure S1.

Slump	Location	Tongue accumulation	**Scar**		**Debris Tongue**	
		(yrs.)	Area (m^2)	Volume (m^3)	Area (m^2)	Volume (m^3)
D1	67.1771° N 135.7555° W	n/a	2,853	-4,565	Not present	Not present
CB	67.1814° N 135.7295° W	<5	34,084	-136,496	12,007	21,567
FM3	67.2539° N 135.2732° W	>10	73,518	-501,916	31,799	147,025
Husky	67.5207 ° N 135.3005 W	>10	64,386	-690,687	73,696	377,666
FM2	67.2545° N 135.2286° W	>30	337,901	-6,003,927	179,000	1,949,711

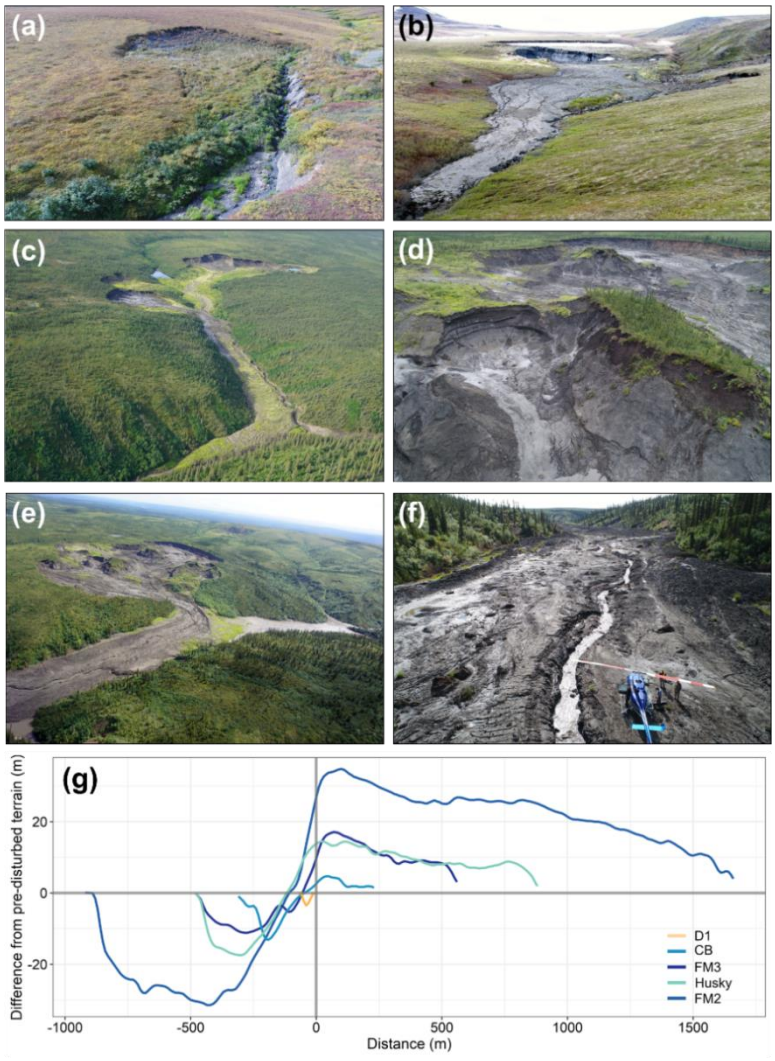

Figure 2. Plate showing retrogressive thaw-slumps, debris tongue deposits and elevation normalized scar-zone and debris tongue profiles for a size and age disturbance continuum, Peel Plateau, Northwest Territories Canada. (a) A small, shallow slope side thaw slump (D1) with vegetated lower slope and active headwall. (b) Oblique photograph of CB in June 2019 showing debris tongue in foreground, secondary slumps on right side of valley, large polycyclic (secondary) headwall in the central scar zone, and small upper (primary) headwall in the background; (c) Husky slump scar and debris tongue, secondary slumps on left, a small debris-dam lake, and slump-drained lake and residual pond to right of upper slump; (d-f) FM2 mega slump and debris tongue. (d) FM2 headwall showing banded relict massive ice and relatively thaw-stable organic deposits and eroded glaciofluvial deposits in upper right (background); (e) FM2 scar area and chute where sediment enters the valley to form the debris tongue and a debris-dam lake, and; (f) the debris tongue surface and the stream channel which has started to incise the deposit. (g) Elevation normalized scar (- values) and debris–tongue (+ values) topographic profiles for slumps and debris tongue deposits. Profiles are differenced from the pre-disturbed terrain surface. Slope transects are from the slump headwall to the intersection with the stream channel, and downstream transects extend to the end of the debris tongue. Slumps and transects are shown in Figure S1.

In 2018, the area of slump FM2 was an order of magnitude larger than the other disturbances, and has been a site of recurrent erosion for over half of a century (Lacelle et al., 2015). About 30% of the scar cavity volume (6.0 x 10^6 m^3) has been accounted for in the valley-fill (Table 1; Figs. 2 d-g), consistent with excess ice content estimates of 50 to 70%. Increasing thaw-driven sediment flows coincided with the regional increase in the frequency and magnitude of thaw slumps in the late 1990s (Kokelj et al., 2015), enlarging the debris tongue to about 2 km length and 35 m thickness by 2018 (Figs. 2 d-g, S1) (van der Sluijs et al., 2018). By filling the trunk valley, these very large deposits flatten the upstream energy profile, creating depositional environments such as the debris-dam lake at FM2 (Fig. 2e), which has infilled with sediment, supplied from erosion of the FM3 debris tongue situated about 1 km upstream. Fluvial incision of the FM2 debris tongue (Fig. 2f) and pinning of the stream channel to the valley wall is causing high rates of erosion. However, the persistence of these thick deposits demonstrates that sediment supply exceeds transport capacity of headwater streams by several orders of magnitude.

3.2 The thaw-driven evolution of slope-to-stream connectivity

The abrupt transition of shallow valley-side thaw-slumps into more dynamic failures that exhibit downstream connectivity is transforming the geomorphology of ice-rich glaciated environments. These dynamics were captured through LiDAR and multi-year UAV observations from Peel Plateau (Fig. 3). Thaw slump CB was initiated by stream erosion around 2002-2004, and gradually back-wasted up an 8 to 12° slope to form a 25,900 m^2 disturbance by 2011, comprised of a shallow scar zone (mean depth = 2.2 m, SD = 2.1 m) with an upper zone of mud slurry and a lower, vegetated accumulation zone (Fig. 3a). The headwall, up to 7.0 m high, exposed the active layer underlain by the early Holocene paleoactive layer and Pleistocene age icy permafrost at depth (Lacelle et al., 2019). In 2015 the scar area had increased to 33,370 m^2 (+29%), but maximum headwall height (5.8 m) and mean concavity depth (1.9 m; SD = 1.9 m) decreased as thawed materials accumulated in the scar zone (Figs. 3b, e). Over the first decade of slump growth material redistribution was constrained largely to the slope system, and top-down thaw of ice-rich permafrost within areas of the lower scar zone is suggested by continued subsidence (Fig. 3b). A major episode of mass-wasting initiated in summer 2017 evacuated the materials accumulated within the slump scar zone to form a 2.2 x 10^4 m^3 debris tongue comprised of colluvium transported up to 200 m down valley, and a ~12.5 m high headwall in the central scar zone concavity. This large, lower headwall observed in fall 2018 exposed about 1 metre of colluvium overlying icy sediments that extended to a depth of at least 14 m below the pre-disturbance surface (Figs. 2b, 3c-e). Gradual retreat of the upper headwall from 2015 to 2018 increased the scar footprint by less than 10%, but evacuation of colluvium in 2017-2018 more than doubled the mean depth and total volume of the scar cavity (Fig. 3). Thaw-driven, rainfall-enhanced re-mobilization of scar-zone colluvium coupled the slope and stream valley by transporting large volumes of erodible substrate into the channel. Evacuation of materials from the scar zone exposed a large secondary headwall strengthening feedbacks that drive slump proliferation (Kokelj et al., 2015).

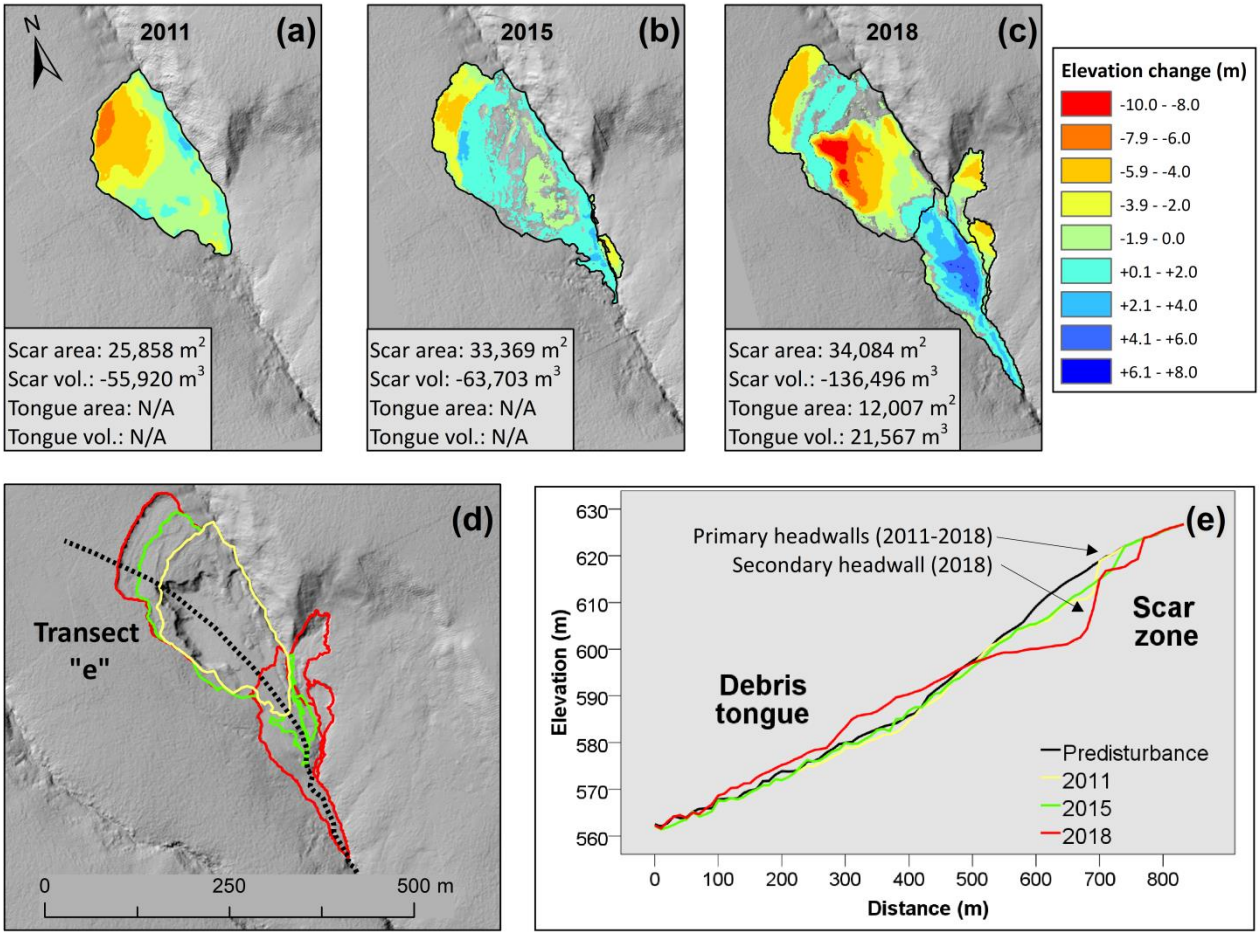

Figure 3. Thaw slump growth (slump CB), material displacement and evolution of downstream connectivity 2011 to 2018, Peel Plateau, Northwest Territories Canada. (a) 2011 difference from the reconstructed pre-disturbance terrain surface; (b) 2015 terrain differenced from the 2011 terrain; (c) 2018 terrain differenced from the 2015 terrain, showing polycyclic behaviour including thaw-driven evacuation of scar materials, and development of a prominent lower "secondary" headwall and scar concavity. Slump and debris tongue area and volumes are calculated relative to estimated pre-disturbance surface. (d) The evolution of thaw slump footprint from 2011 to 2018 and the topographic transect in (e) showing elevation profiles through the slump and along the valley for pre-disturbed terrain, 2011, 2015 and 2018. Hill-shade in (d) is the 2018 UAV survey integrated with the surrounding 2011 regional LiDAR data.

3.3 Quantifying slump enlargement and downstream connectivity across the subarctic to low Arctic transition

Thaw-slump area, volume, maximum concavity depth derived from the 2011 LiDAR study area (Sect. 2.3, Table S1) were compiled to investigate relationships between geomorphology, and downstream connectivity, for the fluvially-incised Peel Plateau and lake-rich Tuktoyaktuk Coastlands and Anderson Plain (Fig. 1). Within the two LiDAR corridors, the digitized scar areas ranged from 242 to 253,900 m^2 with a median of 3,323 m^2. Volume displacement ranged from 130 m^3 to 3,653,400 m^3 with a median of 3,859 m^3, and maximum difference between estimated pre-disturbance surface and disturbed scar surface (referred to as maximum concavity depth) ranged from -1.5 m to -28.0 m with a median of -3.4 m (Table S3). The accumulation of thawed colluvium on the lower slope of smaller slope-side disturbances can produce lobes that manifest as positive relief features (Fig. 3a, b). The larger disturbances were characterized by entirely negative relief relative to the pre-disturbance terrain. The slump size metrics are distributed across 3-4 orders of magnitude in scale, indicating the geomorphic significance of the larger features. T-tests on log-transformed data indicated that the mean of all slump size metrics (area, volume, maximum concavity depth) for the higher relief, fluvially-incised Peel Plateau were significantly greater ($P<0.02$) than in the rolling, lake-rich terrain of the Anderson Plain and Tuktoyaktuk Coastlands.

Thaw slump populations were grouped by their connectivity with the downstream environment. One-way ANOVA indicated significant differences in the means amongst downstream connectivity groups for slump area ($F_{2,\ 68}=32.6$ $P<0.001$), concavity volume ($F_{2,68}=40.9$; $P<0.001$), and maximum concavity depth ($F_{2,\ 68}= 35.2$; $P<0.001$) (Fig. S2). Tukey's HSD post-hoc test indicated significant differences amongst all connectivity groups with disturbance area ($P<0.02$), volume ($P<0.005$) and maximum concavity depth ($P<0.017$) demonstrating that downstream connectivity increases with slump size. This pattern supports Sect. 3.1 and 3.2 indicating that disturbance enlargement is linked to the coupling of slopes and downstream systems.

To further explore the slope-scale geomorphic implications of slump enlargement we examined the relationships between slump scar area and volume, and scar area and maximum concavity depth. A linear model fit through the logarithmically-transformed disturbance area and volume data (Fig. 4a) reveals a power-law relationship ($R^2 = 0.90$; $F=641.9$; $N=71$; $P<0.0001$):

$$(\log \text{Volume}) = -1.44 + 1.42(\log \text{Area}) \qquad \text{(Eq. 1)}$$

The model coefficients are comparable with those describing area-volume relationships of landslide populations for studies from temperate environments across a range of failure mechanisms, material properties and geological settings (Klar et al., 2011). Figure 4b shows the power-law relationship ($R^2 = 0.63$; $F=116.2$; $N=71$; $P<0.0001$) between scar area and maximum concavity depth described by:

(log ConcavityDepth) = -0.76 + 0.36 (log Area) (Eq. 2)

where the depth of permafrost thawed generally increases as thaw slumps enlarge. Residual scatter in both of these relationships reflects inherent differences in landscape, soil properties, geomorphic setting and the stage of slump development (Figs. 2, 3). However, the relationships indicate that slump area can be used to estimate the volume and thicknesses of permafrost thawed, improving our ability to quantify the role of thermokarst mass wasting in landscape evolution. Further investigations are required to determine whether these relationships will vary with landscape, material properties and failure mechanisms.

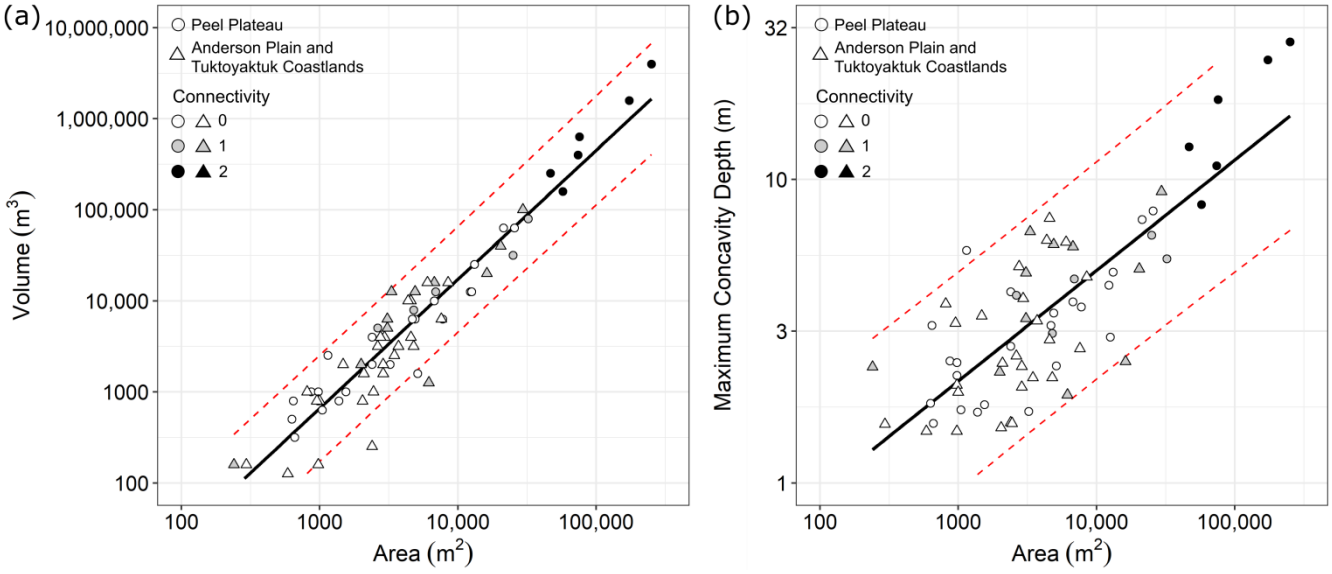

Figure 4. Relationships between: (a) slump scar area and volume (R^2 = 0.90; F=641.9; N=71; P<0.0001), and (b) slump scar area and maximum depth of concavity (R^2 = 0.63; F=116.2; N=71; P<0.0001) for disturbances in the fluvially-incised Peel Plateau, and lake dominated Anderson Plain/Tuktoyaktuk Coastlands. Connectivity between slope and downstream environment is categorized by: 0) no connectivity; 1) physical connection between bare scar and downstream environment; and 2) evidence of downstream deposition of materials into valley, stream channel or lake. Red ~~dotted~~ lines show 95% confidence limit. Regression diagnostics indicate that residuals are normally distributed and there are no unduly influential points.

3.4 Analysis of catchment-scale slope thermokarst effects, Willow River

Thaw-driven mass wasting and slope denudation for 1986-2018 were quantified for the 806 km^2 Willow River catchment (Fig. 1). The fluvially-incised stream network drains ice-rich glacial tills and unglaciated scree slopes of the Richardson Mountains into the Mackenzie Delta. Retrogressive thaw slumps are the dominant mode of slope failure; however extensive field observations confirm that shallow landslides and few large translational failures also occur (Fig. S3) (Lacelle et al., 2010). Bare or sparsely vegetated thaw-slump scar and debris tongues mapped using Landsat imagery (Rudy and Kokelj, 2020) indicated a fourfold increase in the number of active thaw slumps from 1986 to 2002, and another 2.5-fold increase by 2018 (Fig. 5a). These results contrast with earlier assessment by Lacelle et al., (2010) in part due to a larger catchment area in this study, different time scales, and nature of imagery utilized. We employed the empirical models (Fig. 4) to convert digitized slump scar areas to estimates of slump volume and maximum concavity depth for the three time periods. Cumulative disturbance area and volume showed 34 and 80 fold increases over the intervals of record (Figs. 5b, c). The median area of active thaw slump populations for 1986, 2002 and 2018 was 4,510 m^2, 5,680 m^2 and 8,290 m^2, respectively (Fig. 5d, Table S4). Comparison with mean values for the same time periods of 5,000 m^2, 9,770 m^2 and 17,910 m^2 (Table S4) highlights the increasingly skewed nature of the population distributions as disturbances enlarge (Kokelj et al., 2015). Approximated mean slump volumes and maximum concavity depths of active thaw slumps in 1986 were 6,900 m^3, and 3.6 m, increasing to 19,690 m^3, and 4.1 m in 2002 and to 59,030 m^3, and 5.1 m by 2018 (Table S4). The volumes of the largest disturbances have increased by two orders of magnitude, and there has been at least a three-fold increase in maximum concavity depth (Fig. 5), although the models appear to provide conservative high end estimates of both parameters (Fig. 4). Kruskall-Wallis rank sum tests indicated significant differences in slump size indices amongst the different time periods ($\chi^2(2) = 22.825$; $P<0.0001$). Dunn's post-hoc testing showed no significant increases in disturbance area, volume or maximum concavity depth from 1986 to 2002, however increases in the population medians were significant for all size-related indices from the first two time periods to 2018 (Fig. 5d-f; Table S5), suggesting a period of slump initiation followed by accelerated enlargement from about 2002 to 2018. During the 2002-2018 period, development of numerous debris-tongue deposits indicates major strengthening of slope to stream connectivity (Fig. 5a). The catchment-wide cumulative slump volume estimates of 0.15×10^6 m^3 in 1986, 1.43×10^6 m^3 in 2002 and 11.70×10^6 m^3 in 2018 reveal a non-linear increase in thaw-driven geomorphic activity across two orders of magnitude over three decades (Fig. 5c). A significant proportion of volume loss from slopes can be attributed to ground ice melt and water loss, and a large portion of the mobilized slope materials are placed into transient storage in valley bottoms (Fig. 2g). To translate the significant increases in thaw-driven geomorphic activity into values that can be compared with surface denudation rates of catchments in other regions we normalized the combined subsidence and erosional volume losses by catchment area and differenced with the preceding time interval. These calculations indicate that for Willow River watershed, the thaw slump component of surface lowering or volumetric loss amounts to 0.1 mm yr^{-1} or mobilization rates of 100 m^3 km^{-2} yr^{-1} for 1986-2002 and 0.79 mm yr^{-1} or 794 m^3 km^{-2} yr^{-1} for 2002-2018. In a relatively quiescent landscape that is frozen for almost two-thirds of the year, this represents a dramatic change in the geomorphology and sediment delivery regime from thawing slopes to the stream systems.

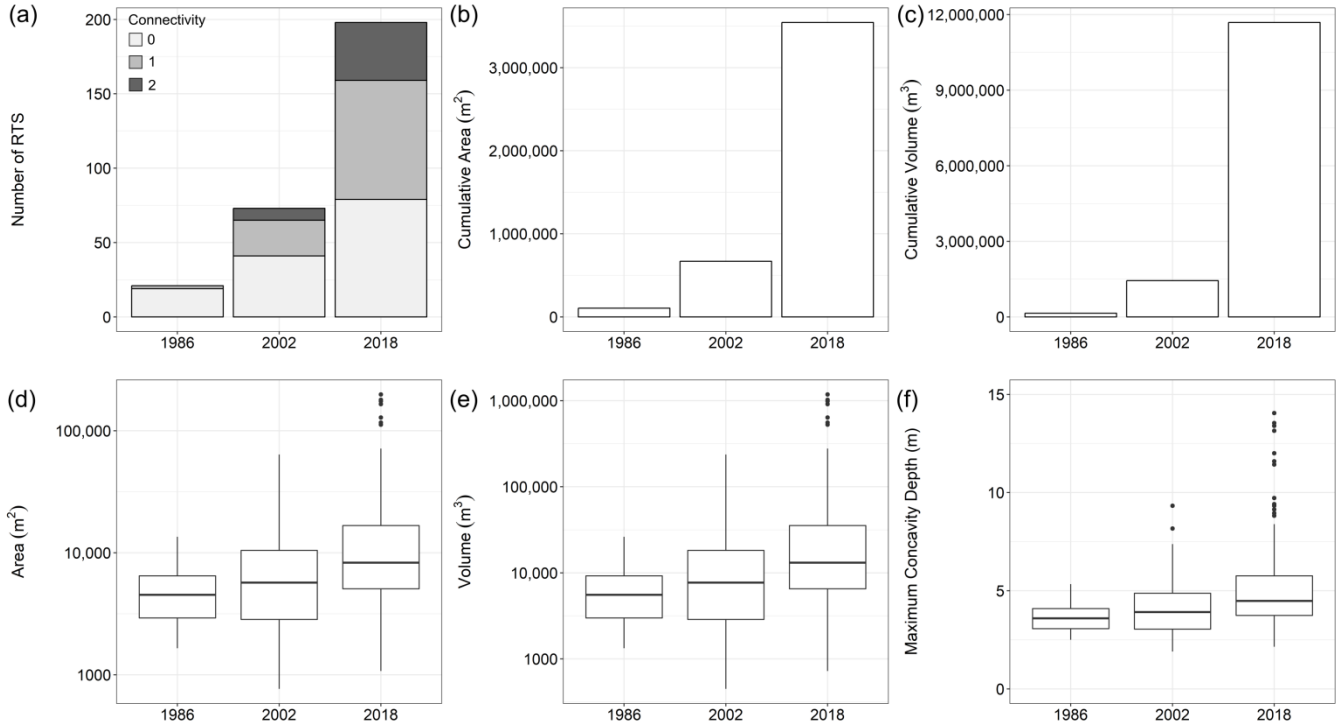

Figure 5. Thaw-driven geomorphic disturbances in the Willow River catchment for 1986, 2002 and 2018. Bar graphs show: (a) Slump counts and connectivity between the slope and downstream environments categorized as 0) no connectivity, 1) physical connection between bare scar area and downstream environment, and 2) evidence of downstream deposition of materials into valley, stream channel or lake; (b) cumulative slump area; and (c) estimated cumulative slump volume. Box and whisker plots showing medians, 25% and 75% quantiles, minimum and maximum values and outliers for: (d) thaw slump area; (e) approximated volumes; and (f) maximum concavity depth. Note logarithmic scale on (d) and (e). Thaw slump volume and maximum concavity thickness estimated using relationships described in Sect. 3.3 and Figure 4. The spatial dataset is available in Rudy and Kokelj, 2020.

The major intensification of thaw-driven mass wasting in the Willow River catchment predominantly occurs on the uppermost slopes in the drainage networks, mainly affecting first and second-order streams (Fig. 6). The exposure of several kilometres of slump headwall confirms that the low-order stream networks are incising ice-rich glaciated terrain and that the majority of materials mobilized by the largest disturbances comprise Pleistocene sediments and relict ground ice (Fig. 6; Video S2). Steeply-incised valley sides of fourth and fifth-order channel segments which occupy the broader valley of Willow River main stem are also affected by a number of large, deep-seated translational failure complexes (Figs. 6, S3) that can exhibit bedrock control, as well as thaw-driven flows. The incised valleys are susceptible to shallow landslides, and although they transfer comparatively modest amounts of sediment to the stream network, they contribute to thaw slump initiation by exposing ground ice on the upper slopes. Our mapping of the Willow River catchment indicates that 116 km out of 861 km of stream segment length were directly affected by ~~slope thermokarst~~ features, with downstream accumulation increasing the length of the affected network by 246 km, to 42% of the entire stream network. The downstream translation of ~~thaw-driven slope sediment mobilization~~ (Figs. 5, 6) through the Willow River fluvial network is indicated by the rerouting of the outflow channel to the Mackenzie Delta in 2007-2008, leading to the rapid infilling of a 3.4 km^2 lake over the span of a decade (Fig. 6c1-2; Video S3).

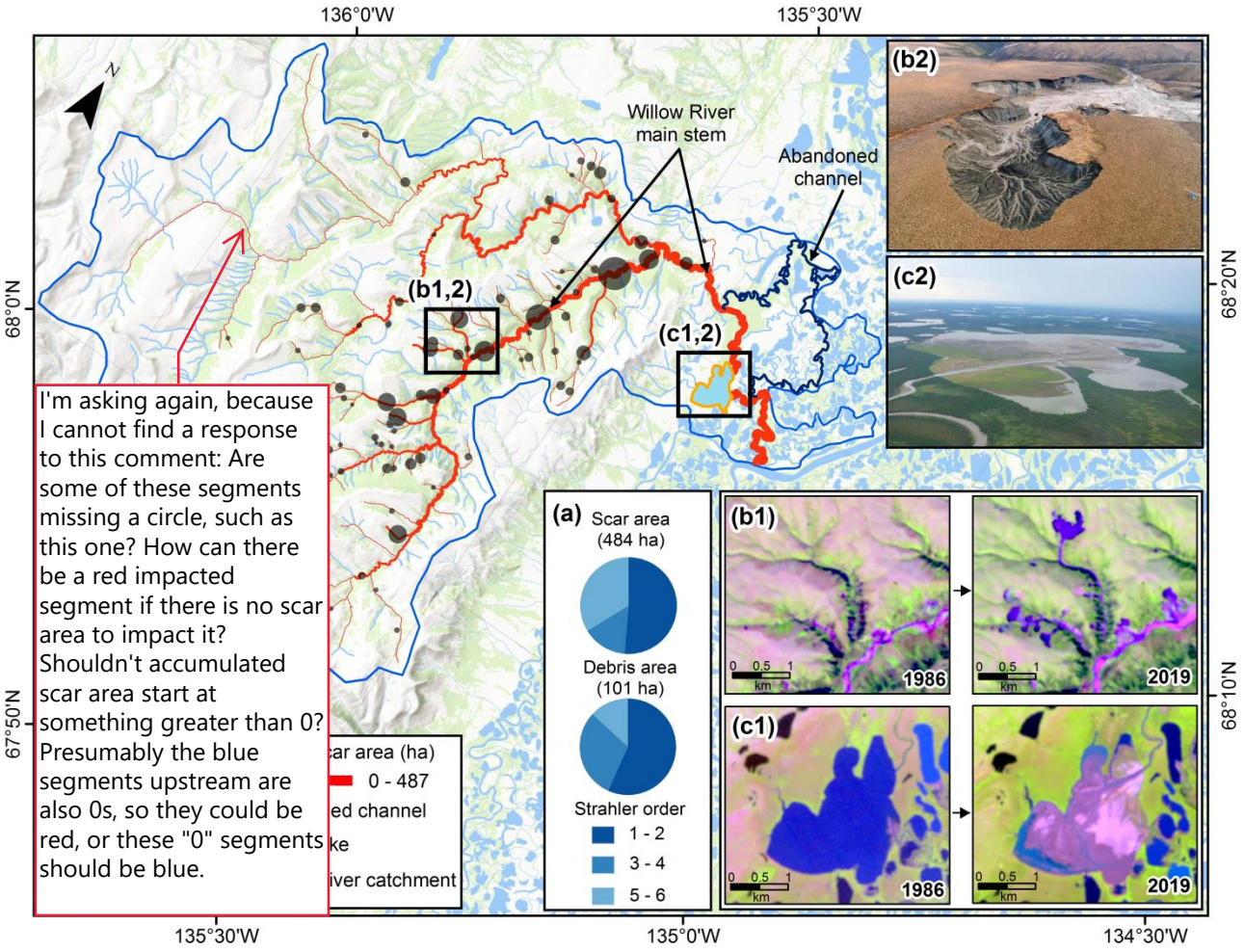

Figure 6. Main map shows thaw-driven landslide impacts to the fluvial network of the Willow River, Mackenzie Delta area. Red lines along the drainage network highlight impacted stream segments, weighted by cumulative landslide scar area (ha), and the downstream accumulation of impacts through the fluvial system. The grey proportional circles indicate the total landslide scar area >1ha per affected stream segment, including thaw slump, and shallow and deep translational slides. Boxes on map labelled (b1, 2) and (c1, 2) indicate inset imagery and photographs. (a) The area weighted distribution of thaw-driven landslide impacts by Strahler order within the Willow River fluvial network. (b1) Landsat images (1986-07-07) and (2019-07-27) indicating increases in thaw-driven landslide erosion since the late 1990s, and (b2) corresponding oblique aerial photograph of the largest thaw slump within the Landsat plate. (c1) Landsat images for the same dates show the lake before and after infilling and delta development where Willow River rerouted in 2007-2008 into Willow Lake, and (c2) oblique photograph of the alluvial deposit. The abandoned channel is shown in dark blue. Base map is from ESRI ArcGIS Online.

3.5 Catchment-scale patterns of thaw-driven mass wasting effects and sediment flux across catchment scales

The patterns of slope thermokarst distribution and intensification were assessed across catchment scales for a 3,520 km^2 area on Peel Plateau and contrasted with a 1,220 km^2 area on southeastern Banks Island (Fig. 1). The distribution of slope disturbance determined from SPOT 4/5 2005-2010 and 2016-2017 Sentinel-2 imagery on Peel Plateau shows increasing frequency across all size classes (Fig. 7a). This pattern reflects initiation of new disturbances, as well as thaw-driven enlargement of existing slope failures. On southeastern Banks Island, overall slope disturbance density was greater, but the relative increase over the past decade was lower than for Peel Plateau. A distinct shift towards larger thaw slumps on Banks Island suggests disturbance growth and coalescence (Fig. 7b). Figure 7c provides a cumulative summary of the points at which the river network is being impacted by thaw-driven mass wasting. Evidently thaw slumps and slides tend to impact the channel at 1-100 km^2 catchment scales, consistent with patterns observed for Willow River (Fig. 6a). The temporal shift from 2005-2010 to 2016-2017 towards a relative increase in direct effects to larger channels in the Peel Plateau region reflects the greater watershed sizes, and thus more available downstream terrain for new disturbance impacts (Fig. 7c). Some of the main Peel River tributaries are increasingly being affected by large slope thermokarst failures and shallow slides (Figs. 6, S3). On Banks Island, the smaller fluvial networks were already highly impacted by thaw slumping in 2005 (Segal et al., 2016a, Lewkowicz and Way, 2019), leaving less available terrain for expansion of direct network impacts, as indicated by smaller increases in slump incidence (Fig. 7b), and a static pattern in distribution of catchment disturbances between the two time periods (Fig. 7c). Figure 7d reinforces that the geomorphic and geochemical impacts to headwater streams tend to be more intense than direct impacts to larger systems, because the size of the disturbance relative to the watershed area will be far greater. Further downstream, the overall impacts from individual disturbances and cumulative effects will be proportionately less, given the much larger upstream catchment area and greater stream transport capacity, relative to sedimentary or geochemical yields from the disturbance.

There is a notable dearth of river sediment monitoring over the vast, thermokarst sensitive regions of northwestern Canada. A compilation of available grab samples of stream sediment concentrations coinciding with discharge measurements within and adjacent to Peel River basin for catchments from 10^{-1} to 10^4 km^2 indicates a negative trend in specific low-flow fluxes with catchment area. Estimates of low-flow sediment fluxes for small catchments affected by thaw-driven mass wasting are up to two orders of magnitude greater than for larger watersheds, and several orders of magnitude greater than for undisturbed and unglaciated catchments (Fig. 7e).

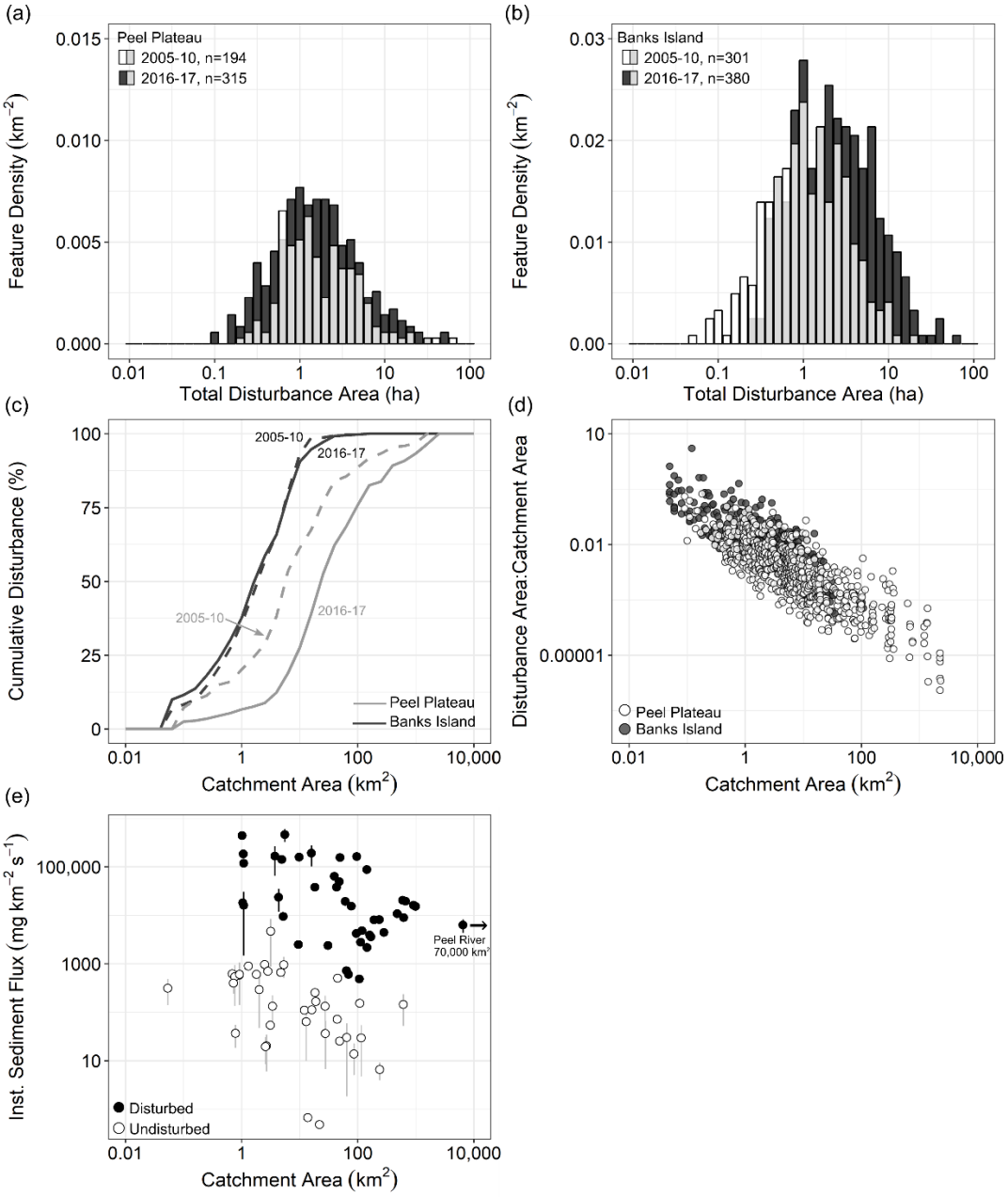

Figure 7. The patterns of slump intensification in fluvial networks for 2005-2010 and 2016-2017 in Peel Plateau (3,520 km^2) and eastern Banks Island (1,220 km^2) regions. (a, b). Size distribution of thaw slumps for the two time periods where white indicates 2005-2010, black indicates 2016-2017, and shading shows overlap between 2005-2010 and 2016-2017 distributions; (c) Cumulative count of thaw slumps plotted against upstream catchment area; (d) The ratio of disturbance area to upstream catchment area plotted against upstream catchment area; and (e) July-September instantaneous sediment flux rates for streams of the Peel watershed and adjacent areas.

3.6 Thaw-driven mass wasting effects propagate through hydrological networks to the ocean

Here we project the potential cascade of slope thermokarst effects through Arctic drainage networks from continuous permafrost of northwestern Canada (Fig. 8). The summary of active permafrost landslides by Strahler stream order for Banks Island (70,794 km^2), Amundsen Gulf (90,288 km^2), Peel River (76,506 km^2), and Keele/Redstone (39,957 km^2) watersheds indicates that the greatest abundance and highest density of directly affected stream segments was on Banks Island (11.8/1000 km^2) and the lowest was in the Amundsen Gulf (2/1000 km^2). However, major thermokarst hotspots associated with ice-rich moraine, glaciofluvial and glaciolacustine materials occur within all four watersheds where slope disturbance densities are an order of magnitude greater than the watershed average. About 71% of direct thaw-driven mass wasting effects to streams, and over 81% of direct effects to lakes occur within first and second order hydrological segments (Fig. 8a), corroborating catchment-scale patterns (Figs. 6, 7), and indicating that thousands of small streams and hundreds of lakes across northwestern Canada are directly affected by slope thermokarst disturbances (Fig. 8b). The main impacts of thaw-driven mass-wasting on hydrological networks are concentrated in well-defined geographical areas, with large regions free of major slope thermokarst. For Banks Island and the Peel and Keele-Redstone watersheds, low disturbance densities occur west of the late Wisconsinan ice-limit. Thaw-driven landslides were sparse in unglaciated Cordilleran areas and glaciated Precambrian Shield with patchy till veneer. Low disturbance density also characterizes the Taiga Plains of central Mackenzie Valley, however some valleys incised in tills and glaciolacustrine deposits are prone to thaw-related failures, including the Mackenzie River main stem (Figs. 8, S4iii).

As a broad summary, ~~slope thermokarst~~, directly affects over 6,750 km of stream segment length, 1,370 lakes and about 900 km of coastline in the continuous permafrost drainage of northwestern Canada (Fig. 8). About 48,800 km of stream network and over 5,600 lakes are susceptible to downstream effects, reflecting 7.2- (streams) and 4.1- (lakes) fold increases over the extent of direct hydrological effects. The much greater extents of downstream effects (Fig. 8a) occur because thermokarst mass wasting predominantly impacts low-order streams often in headwaters of the hydrological network. A high density of thaw slumps affecting small streams that drain eastern Banks Island and northwestern Victoria Island indicate major propagation of sedimentary and geochemical effects directly to the coastal zones of the Prince of Wales Strait (Fig. 8). Northeast of the Mackenzie Basin several major Arctic river catchments have areas of high landslide density with the potential to propagate downstream effects. Ice-rich glacigenic deposits of Anderson Plain and Tuktoyaktuk Coastlands surround the Husky Lakes estuary, which is influenced by shoreline slumping, discharge from numerous small slump-affected, lake-dominated catchments, and a few slump-affected northward-flowing rivers, indicating a regional hotspot of accumulated effects (Figs. 8, S4ii). Coastal slumping along the Yukon North Slope and uplands east of Mackenzie Delta, in conjunction with lake-side slumps comprise the majority of mass-wasting processes there, whereas fluvial transfer from inland impacts to the coast is limited. High densities of thermokarst mass wasting affect numerous fluvial-incised networks draining ice-rich glaciated landscapes of the lower Mackenzie and Peel River basins, so these two major rivers propagate the greatest magnitude of thaw-driven sedimentary and geochemical effects to the Mackenzie Delta and Beaufort Sea (Fig. 8).

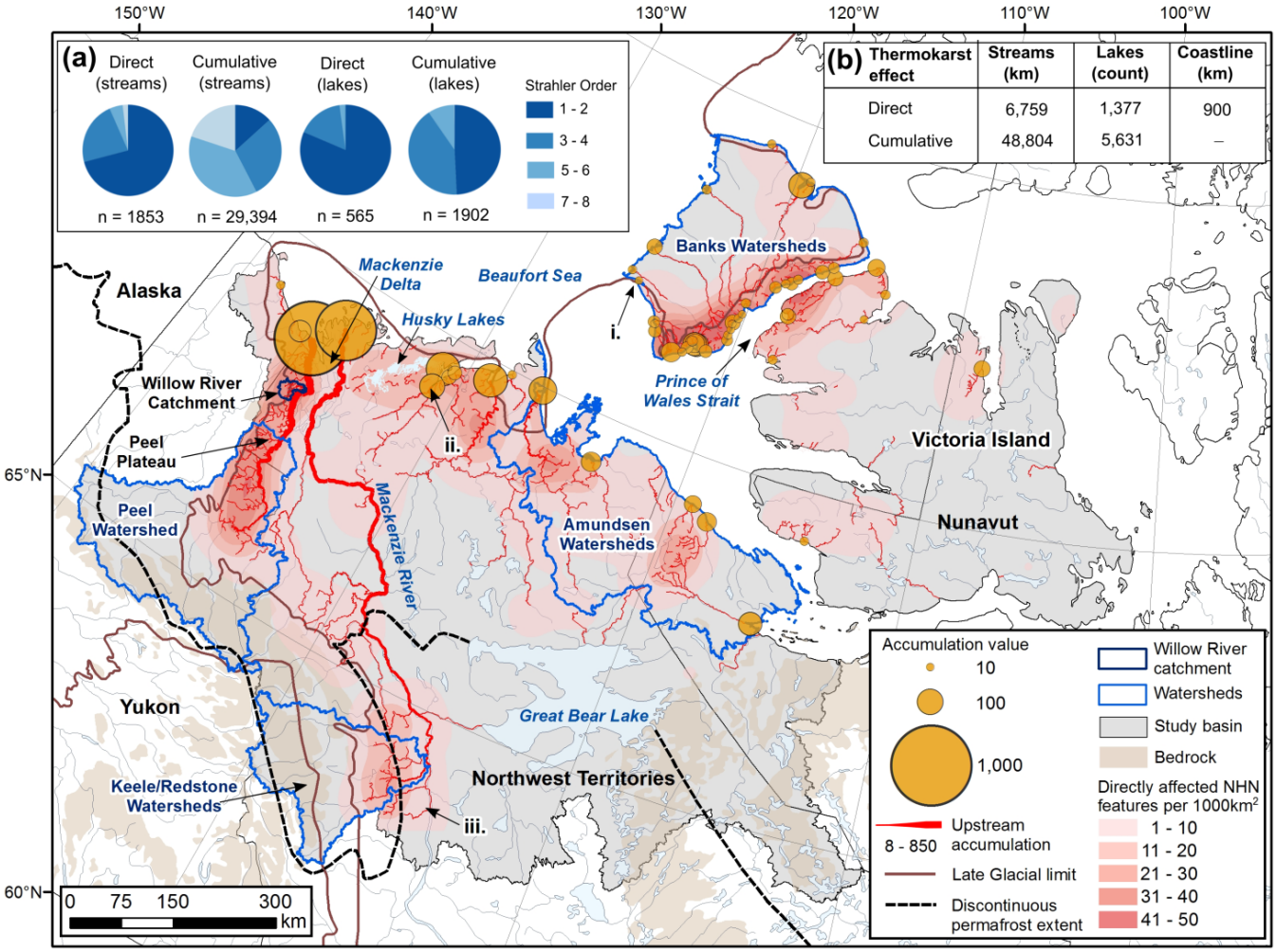

Figure 8. Thaw-driven landslide density and downstream accumulation of effects, western Canadian Arctic drainage from continuous permafrost terrain. Heat map depicts all directly affected stream, lake and coastal hydrological features mapped. All upstream accumulation values shown within the fluvial network are >2 and at the coast are >9. Accumulated effect contributions of the Mackenzie and Peel Rivers to the Beaufort Sea are routed separately for comparison. (a) Counts of direct and accumulated thaw-driven mass wasting effects to fluvial systems by Strahler order for the four major watersheds outlined in blue. (b) Table showing lengths of directly affected hydrological network and accumulated effects, count of directly and indirectly affected lakes and total directly affected coastline for western Arctic drainage from continuous permafrost. Remote sensing examples of thaw-driven downstream sedimentation provided in Fig. S4 for: i) Sachs River and Fish Lake, ii) Miner River inflow to the Husky Lakes estuary and iii) massive deep-seated permafrost failure on Johnson River. Late glacial limit is from Dyke and Prest, 1987, bedrock geology is from Fulton, 1995, and the permafrost boundary is from Brown et al., 1997. Base map is from ESRI ArcGIS Online.

4 Discussion

4.1 Thresholds and connectivity between slopes and downstream environments

Results indicate that intensification of thaw-driven mass wasting is altering the Holocene-scale regime of sediment production, mobilization, and delivery in glacially-conditioned permafrost landscapes of northwestern Canada (Figs. 2, 3, 6, 7e, S4). Hillslope-channel coupling is increasing as slope thermokarst disturbances evolve into multi-decadal, thaw-driven conveyors of fine-grained sediment and solutes to downstream environments. Slope morphology and sediment yields in unaffected catchments and the absence of relict valley fills suggest that over the past millennia, material redistribution associated with most slope failures was restricted to the slope system (Figs. 2a, 3a, b). Exceedance of critical thresholds controlling sediment detachment from hillslopes driven by interdependent factors of warming, precipitation, permafrost thaw and soil saturation (Lewkowicz and Way, 2019; Segal et al., 2016a; Ward-Jones et al., 2019) have instigated processes and feedbacks (Figs. 2, 3) (Kokelj et al., 2015), rapidly mobilizing materials and coupling slopes with hydrological systems across many glacially-conditioned permafrost environments (Figs. 5-8). The non-linear growth of disturbances, strengthening of downstream connectivity (Figs. 2-4), and predominant impacts to low-order streams (Figs. 7c-e, 8a) emphasizes that increasing disturbance size is having a disproportionate effect on the magnitude and duration of downstream effects.

Recent thaw-driven mobilization of slope materials has increased storage in valley bottoms by several orders of magnitude, forming large valley fills (Figs. 2, 3), and together with the steepening and lateral displacement of channels, will amplify fluvial sediment transport for decades to centuries. Slope-to-channel coupling is particularly enhanced in steeply incised and confined valleys, so that environments like the Peel Plateau have emerged as hotspots of geomorphic change and downstream effects (Figs. 6, 8) (Kokelj et al., 2013; Zolkos et al., 2018). The transition from the long-term 'supply-limited' norm of Holocene permafrost geomorphic systems (*sensu* Carson and Kirkby, 1972; Howard, 1994), is striking. The change is emphasized by the unprecedented climate-driven sediment mobilization from long-frozen slopes rapidly overloading a network of newly "under fit" streams (Figs. 2, 3, 6). Enhanced slope-channel coupling is evident across the study region, however, the downstream conveyance of sediment and geochemical effects will vary (Shakil et al., 2020a), because the connectivity of slope and hydrological systems are inherently sensitive to substrate and geochemical properties, network configuration, stream power, physiography, permafrost conditions and climate drivers. While it is difficult to translate thousands of discrete and dynamic slope disturbances into coherent estimates of river impacts at the basin-scale, this is a central challenge facing periglacial geomorphologists, biogeochemists and aquatic ecologists in the Anthropocene.

4.2 Non-linear disturbance trajectories

The thickness of materials mobilized by thaw-driven mass wasting is associated with disturbance volume, and both parameters relate to thaw-slump area via power-law relationships (Sect. 3.3; Fig. 4). The area-volume model we derived has

690 coefficients closely comparable to landslide populations in temperate environments (Klar et al., 2011). These relationships are complex because permafrost, geomorphic, and climatic factors influence the growth trajectories of thaw-driven slope disturbances (Figs. 2, 3), producing diverse and dynamic morphologies over different terrains. Regardless, these relationships provide a first empirical basis for estimating thaw-driven denudation as a function of disturbance area (Figs. 4, 5, 7a), and better approximation of the geomorphic, sedimentary, geochemical and carbon consequences of intensifying
695 slope disturbance regimes. Further studies are required to determine the potential variability in area-volume relationships with landscape type, slump development stage, material properties and different failure modes.

Rapid increases in the area of thaw-driven slope disturbances have a major influence on terrain evolution, and downslope sediment and geochemical mobilization. Increasing prominence of larger and proportionately deeper disturbances indicates
700 greater volumetric permafrost thaw and sediment mobilization than would occur for the equivalent, combined surface area of numerous small slumps (Fig. 4; Table 1, 2). This also suggests that a greater range of material types are likely to be thawed and entrained (Fig. 2). In glacigenic deposits, materials excavated from deeper in the soil stratum have lower organic matter contents and are unlikely to have been subject to thaw-induced geochemical changes that characterise the active layer and near-surface permafrost (Lacelle et al., 2019). Enlargement and accelerated back wasting of the slump headwall, coalescence
705 of thaw slumps, and polycyclic behaviour (Figs. 2, 3) increase the production of saturated substrate and the probability of material evacuation from the scar zone. As the magnitude of thaw-driven slides increases there is also greater potential for bedrock, or in southern permafrost regions, unfrozen materials, to be exposed, expanding the range of geomorphic and geochemical effects, and linkages between surface and subsurface flow paths (Walvoord and Kurylyk, 2016).

710 The intensification of thaw-driven mass wasting is inextricably linked with the strengthening of downstream connectivity (Figs. 2, 3, 4; Tables 2, 3). For example, as retrogressive thaw-slumps enlarge, greater volumes of material, varying laterally and stratigraphically are mobilized, mixed as a saturated slurry, and transported by a suite of mass-wasting processes to form colluvial deposits that can veneer slopes, accumulate in downstream environments or enter larger river channels, as well as lacustrine or coastal environments (Figs. 2, 3, S1) (Kokelj et al., 2015; Houben et al., 2016; Ramage et al., 2018). Debris
715 tongue development in small streams is also commonly blocking drainage and causing lakes and ponds to form at hundreds of locations (Fig. 2, S4ii, iii). The rapid intensification of thaw-driven mass wasting combined with variation in the type of landscapes being impacted, and the nature and magnitude of material mobilized, has a range of geomorphic, biogeochemical and ecosystem implications that require study (Tank et al., 2020; Vonk et al., 2019) so that the consequences can be predicted in an informed manner.

720

4.3 The river network: transfer of thermokarst erosional materials from source to sink

This spatially-nested study provides several insights on the evolving nature of slope-thermokarst and the effects on hydrological networks. Firstly, acceleration of thaw-driven mass wasting is affecting thousands of first and second-order

lakes and streams in glacially-conditioned permafrost landscapes (Fig. 8). Major sedimentary, geochemical and ecosystem impacts upon low-order stream networks have been abrupt because the magnitude of disturbance and enhancement of downstream connectivity facilitate propagation through small systems with an inherently limited capacity to absorb disturbance (Figs. 7c, d). Thaw-driven mass wasting can entirely change the character of the stream reach (Figs. 2, 3, S4ii, iii), the sediment and geochemical fluxes (Fig. 7e) (Kokelj et al., 2013; Shakil et al., 2020a), and the associated habitat potential (Chin et al., 2016). Secondly, thaw-driven sediment and geochemical mobilization is directly impacting, or accumulating to affect thousands of low-order lakes in glacially-conditioned environments (Fig. 8) that are also inherently predisposed to abrupt limnological responses (Houben et al., 2016; Kokelj et al., 2009). Thirdly, slope thermokarst predominantly occurs in at the 10^{-1} to 10^{2} km^2 catchment scales where the geomorphic impacts are prolific (Figs. 5-7). Through tracking changes in the size and distribution of thaw slump features within the Willow River study catchment, we estimated a two order-of-magnitude increase in thaw-driven mass wasting from 1986 to 2018 (Figs. 5a-c). Through integrating sediment and ground ice loss, we estimate about an order of magnitude increase in the contribution to catchment-scale denudation, from 0.1 mm yr^{-1} (1986-2002) to 0.8 mm yr^{-1} for the 2002-2018 period (Figs. 5, 6). Fourthly, fluvial networks integrate a time-transient cascade of watershed effects indicating that water quality, aquatic ecosystems, and fish habitat will be affected across increasingly larger river systems and coastal environments in the study domain (Fig. 8). Hillslopes along higher order channels are also subject to the direct effects of thaw-driven landslides, resulting cumulative sedimentary and geochemical effects on larger systems (Figs. 6, S3, S4). Unequivocal evidence that thermokarst-derived sediments in addition to geochemical effects are propagating through fluvial networks is provided by channel re-routing and rapid infilling of a large lake where the Willow River discharges to Mackenzie Delta (Fig. 6; Video S3), and by the increases in turbidity of numerous downstream lake, delta, estuary, and coastal environments (Fig. S4), which coincide with our predicted areas of downstream accumulated effects (Fig. 8).

4.4 Hydrological connectivity defines a significant global change hotspot

The significance of thaw-driven mass wasting is magnified by the propagation of sedimentary and geochemical effects to freshwater systems and the marine environment (Ramage et al., 2018; Rudy et al., 2017a; Vonk et al., 2019). While we have not simulated dynamic routing of sediment across the 1,000,000 km^2 study area, our nested design demonstrates evolving linkages between slope thermokarst and hydrological systems (Figs. 2-8). Rapid proliferation of numerous, major point source disturbances amplifies the potential of downstream cumulative effects as mobilized sediments, solutes, and carbon transit a sequence of storage reservoirs, and reinforce a thermokarst signal that is projected to cascade across increasing watershed scales to marine environments through the coming century. Although this broad-scale analysis (Fig. 8) neglects relative disturbance intensity, geomorphic and biogeochemical sinks, the variation in slope-downstream connectivity, and transport gradients, it provides a spatially explicit framework for exploring the distribution and propagation of thermokarst effects through hydrological networks. Identification of thaw-driven sediment and solute source areas, and the primary

hydrological networks that convey slope thermokarst effects to coastal environments, emphasizes the interconnected nature of this globally significant thermokarst hotspot (Fig. 8), and could guide future scientific investigations in the study region.

4.5 Glacial legacy controls intensity of thaw-driven mass wasting and impacts to fluvial networks

Glacial legacy, geomorphic setting, and climate history combine to determine the distribution and intensity of thaw-driven mass wasting, and the nature and routing of downstream effects across continuous permafrost of northwestern Canada (Figs. 1, 8) (Kokelj et al., 2017a). A cooling trend through the Holocene (Porter et al., 2019) preserved ground ice and maintained moraine, glaciofluvial, glaciolacustrine, and glaciomarine deposits in a quasi-stable state. Climate-driven episodes of permafrost thaw, most notably in the early Holocene, have left their imprint in the form of ancient landslide scars, thaw lakes, colluvial deposits, and a regional thaw-unconformity (Burn, 1997; Lacelle et al., 2019; Mann et al. 2010; Murton, 2001). However, millennia of cold-climate constraints on slope evolution and fluvial network development are made apparent by the abundance of steeply incised, or solifluction-smoothed valley slopes underlain by ice-rich permafrost, and now juxtaposed with adjacent, increasingly large climate-driven mass wasting features that are mobilizing large volumes of materials that far exceed the transport capacity of low-order streams (Figs. 2, 3, 5, 6). In continuous permafrost regions, climate-driven rejuvenation of post-glacial permafrost slope evolution is driven primarily by top-down thawing causing shallow sliding and thaw slump development (Figs. 1, 2, 5, 6) (Lewkowicz and Way, 2019; Segal et al., 2016a; Ward-Jones et al., 2019). However, ground warming and a loss of soil strength at depth have also led to increasing frequency and magnitude of deep-seated rotational and translational slope failures in low and subarctic environments (Figs. S3, S4iii) (Aylsworth et al., 2000; Young et al., 2020). The intensification of precipitation regimes throughout parts of the study area has increased thermoerosion, shallow landsliding, and downslope sediment transfer in active thaw slumps so that thawing slopes are increasingly pushed toward an unstable state (Fig. 2) (Kokelj et al., 2015). In the subarctic, ecosystem disturbances such as fire compound effects of climate warming (Holloway et al., 2020), triggering an array of slope mass-wasting processes in areas already predisposed to slope instability (Fig. 8). ~~Several feedbacks could counteract the~~, present intensification of thaw-driven mass wasting and increasing sedimentary and geochemical fluxes, ~~including~~ climate cooling, exhaustion of sediment supply and progressive loss of ground ice from the most sensitive slopes, and gradual thaw-driven decreases in slope gradients, however these ~~factors~~ are most relevant at centennial time-scales or greater.

The most intensive slope thermokarst activity in North America, and perhaps across the circumpolar Arctic, has been associated with western margins and recessional positions of the Laurentide ice-sheet (Figs. 1, 8) (Kokelj et al., 2017a) where preservation of relict segregated and glacier ice (Lacelle et al., 2010; Lakeman and England, 2012; Mackay, 1971; Murton et al., 2005) and aggradation of Holocene ground ice (Burn, 1997; Holland et al., 2020) is hosted within thick glacigenic deposits. These ice-rich glacial materials are derived largely from Paleozoic and Cretaceous sedimentary rocks, and the majority of the deposits include fine-grained, solute-rich materials, easily mobilized by thaw-driven slope failure and fluvial processes (Figs. 2-3, 6, S4). These environments stand in contrast to the relatively stable slopes of glaciated terrain in

shield dominated landscapes in southeastern portions of this study region. Areas of uplifted and incised glaciomarine deposits also fit within the framework of permafrost preserved glacially-conditioned landscapes, and although many are outside of our study domain, significant terrain, sedimentary and geochemical responses to thawing slopes have been documented there (Kokelj and Lewkowicz, 1999; Ward-Jones et al., 2019).

The rapid intensification of thaw-driven mass wasting and the patterns of impacts across fluvial networks of northwestern Canada indicate a deglaciation-phase response pattern (Figs. 2, 6-8), which reflects a typically abrupt period of geomorphic transition (Ballantyne, 2002), that in permafrost regions has experienced a long-term climatic hiatus through a cooling Holocene. While more data are needed to describe the full spectrum of annual fluvial sediment yield across catchment scales in thermokarst-affected landscapes, there is a consistent pattern of much higher fluxes in headwater systems, the site of 'primary' glacial sediment stores (*sensu* Ballantyne, 2002). This pattern in thermokarst affected permafrost regions contrasts with that found in temperate British Columbia's post-glacial river systems, where primary glacigenic sediment stores have been exhausted: those materials have cascaded through fluvial networks over millennia and are now reworked and transported by larger rivers (>1,000 km^2; Church and Slaymaker, 1989). In glacially-conditioned permafrost landscapes, climate-driven thaw of glacial sediment stores is overwhelming the transport capacity of low-order streams, leading to valley-filling, upstream pond and lake formation, and river aggradation that will reinforce this early-stage paraglacial signal for centuries to come. The prospect that climate-change is renewing the sequence of post-glacial landscape evolution points to the massive potential for thermokarst-driven geomorphic change of ice-rich slopes, and the centennial to millennial scale perturbation of downstream fluvial systems (i.e., Church and Slaymaker, 1989) and the receiving lacustrine, deltaic and coastal environments in several Arctic regions (Kokelj et al., 2017a).

5. Conclusions

Non-linear intensification of thaw-driven mass wasting is transforming permafrost preserved glacigenic landscapes and downstream connectivity, triggering a cascade of effects that are propagating through Arctic hydrological networks. In the most intensely impacted watersheds, hundred-fold increases in thaw-driven geomorphic activity have been quantified over a three-decade period. Power-law relationships between thaw slump area and volume emphasize the non-linear influence of increasing disturbance area on landscape morphology, slope to stream connectivity and downstream effects. The disequilibrium imposed by thaw-driven release of glacigenic sediment stores from the headwater slopes (1st and 2nd-order streams) reflects a tipping point within these permafrost land systems and signals decadal to millennial scale perturbation of downstream hydrological networks.

We estimate that thaw-driven mass wasting directly affects approximately 6760 km of stream segments, 1380 lakes, and 900 km of coastline across the 994,860 km^2 Arctic drainage area ~~from~~ continuous permafrost of northwestern Canada. The propagation of thermokarst effects through fluvial networks has the potential to increase the number of affected lakes by at

least a factor of 4.0, and the length of the impacted fluvial network by a factor of 7.0. Projection of accumulated slope thermokarst effects indicated numerous susceptible lake, delta, estuary and coastal environments throughout the study basin. Major thaw-driven geomorphic activity is concentrated along ice-rich moraine systems that define coastal regions of Banks and Victoria Island bounding Prince of Wales Strait where numerous, small, intensely affected fluvial systems transfer thermokarst-derived sediments and solutes short distances to the coastal environment. In contrast, the thaw-driven sediment and solute loads conveyed by hundreds of upland streams draining glaciated, ice-marginal landscapes of the lower Peel and Mackenzie watersheds are routed into the two major rivers and indicate a centennial to millennial scale cascade of thermokarst effects to the Mackenzie Delta and the Beaufort Sea. The varying intensity of thaw-driven slope disturbances and the propagation of sedimentary and biogeochemical effects (i.e., dissolved vs. particulate; carbon vs. nutrients vs. major ions) across hydrological networks of varying configuration (e.g., channel slope, lake density, size) will define the evolution of downstream geomorphic, ecological and biogeochemical systems over the coming centuries.

Glacially-conditioned permafrost terrain exhibits exceptionally strong climate-geomorphic linkages and massive potential for thaw-driven geomorphic transformation. Intensifying slope thermokarst effects are propagated through hydrological networks amplifying the extent, magnitude and duration of impacts related to permafrost thaw. Through placing thaw-driven geomorphic phenomena in a geological and hydrological framework, spatial patterns and trajectories of landscape change, as well as environmental consequences can be contextualized and predicted in an informed manner. Glacial legacy, rejuvenation of post-glacial permafrost landscape evolution, and patterns of continental drainage dictate that western Arctic Canada will be an interconnected thermokarst hotspot of global significance through the coming millennia.

Data availability. Datasets used in this publication and sources are summarized in Table S1. Framework and geoprocessing steps for developing flow accumulation analysis are available in the Supplementary materials.

Supplementary materials. The supplement related to this article is available online at: https://tc.copernicus.org/preprints/tc-2020-218/tc-2020-218-RC2-supplement.pdf

Author contributions. SVK and JT developed the paper concept. All authors contributed to field data collection and analysis of data and refinement of paper scope. JV processed the UAV and LiDAR and conducted statistical analyses on the datasets with input from SVK and JT. JK and SVK developed the flow network analysis with input from JT and AR. AR, JV and JK produced final figures. SVK drafted and revised the paper with input from all authors.

Competing interests. The authors declare that they have no conflict of interest.

Acknowledgements. The work has been funded by the Department of Environment and Natural Resources Climate Change and Northwest Territories Cumulative Impact Monitoring Program of the Government of the Northwest Territories, the Natural Science and Engineering Research Council of Canada, and the Polar Continental Shelf Program, Natural Resources Canada. Institutional support from the Tetl'it and Ehdiitat Renewable Resource Councils, the Inuvik, Tuktoyaktuk and Sachs Harbour Hunters and Trappers Committees, the Inuvialuit Joint Secretariat, the Inuvialuit Land Administration, the Aurora Research Institute and the NWT Centre for Geomatics have been critical to the success of this research program. Field support from Christine Firth, Eugene Pascale, Steven Tetlitchi, Alice Wilson, and Billy Wilson are gratefully acknowledged. We would also like to acknowledge reporting of major landslide incidents from Donald Arey, Douglas Esagok, Eric McLeod and Connor Gould. Photographs in Figure 2 were provided courtesy of Rob Fraser, Canada Centre for Remote Sensing. This research has benefited from discussions with Chris Burn, Douglas Esagok, Rob Fraser, Denis Lacelle, Trevor Lantz, Peter Morse and Stephen Wolfe. Thoughtful and detailed comments by Stephan Gruber, Julian Murton and Ingmar Nitze have improved this manuscript.

References

Abbott, B. W., Jones, J. B., Godsey, S. E., Larouche, J. R., and Bowden, W. B: Patterns and persistence of hydrologic carbon and nutrient export from collapsing upland permafrost. Biogeosciences, 12, 3725–40, https://doi.org/10.5194/bg-12-3725-2015, 2015.

Aylsworth, J. M., Duk-Rodkin, A., Robertson, T., and Traynor, J. A.: Landslides of the Mackenzie Valley and adjacent mountainous and coastal regions, in: The Physical Environment of the Mackenzie Valley: A Baseline for the Assessment of Environmental Change, edited by: Dyke, L. D., and Brooks, G. R., Geological Survey of Canada Bulletin 547, 167-176, https://doi.org/10.4095/211888, 2000.

Ballantyne, C. K.: Paraglacial geomorphology. Quaternary Sci. Rev. 21, 1935–2017, https//doi.org/10.1016/S0277-3791(02)00005-7, 2002.

Balser, A. W., Jones, J. B. and Gens, R.: Timing of retrogressive thaw slump initiation in the Noatak Basin, northwest Alaska, USA J. Geophys. Res. Earth Surf. 119, 1106–20, https://doi.org/10.1002/2013JF002889, 2014.

Bater, C. W. and Coops, N. C.: Evaluating error associated with lidar-derived DEM interpolation. Computers & Geosciences, 35(2), 289-300, https://doi.org/10.1016/j.cageo.2008.09.001, 2009.

Beel, C. R., Lamoureux, S. F., and Orwin, J. F.: Fluvial response to a period of hydrometeorological change and landscape disturbance in the Canadian High Arctic. Geophys. Res. Lett., 45, https://doi.org/10.1029/ 2018GL079660, 2018.

Boreggio, M., Bernard, M., and Gregoretti, C.: Evaluating the Differences of Gridding Techniques for Digital Elevation Models Generation and Their Influence on the Modeling of Stony Debris Flows Routing: A Case Study From Rovina di Cancia Basin (North-Eastern Italian Alps). Frontiers in Earth Science, 6, 89, https://doi.org/10.3389/feart.2018.00089, 2018.

Bowden, W. B., Gooseff, M. N., Balser, A., Green, A., Peterson, B. J., and Bradford, J.: Sediment and nutrient delivery from thermokarst features in the foothills of the North Slope, Alaska: Potential impacts on headwater stream ecosystems. J. Geophy. Res. Earth Surf. 113, G02026, https://doi:10.1029/2007JG000470, 2008.

Brooker, A., Fraser, R. H., Olthof, I., Kokelj, S. V., and Lacelle, D.: Mapping the activity and evolution of retrogressive thaw slumps by tasselled cap trend analysis of a Landsat satellite image stack. Permafrost Periglac., 25 243–56, https://doi.org/10.1002/ppp.1819, 2014.

Brown, J., Ferrians, O.J., Heginbottom, J. A., and Melnikov, E. S., eds.: Circum-Arctic map of permafrost and ground-ice conditions. Washington, DC: U.S. Geological Survey in Cooperation with the Circum-Pacific Council for Energy and Mineral Resources. Circum-Pacific Map Series CP-45, scale 1:10,000,000, 1 sheet, https://doi.org/10.3133/cp45, 1997 (revised 2001).

Burn, C. R.: Cryostratigraphy, paleogeography, and climate change during the early Holocene warm interval, western Arctic coast, Canada. Can. J. Earth Sci., 34, 912-925, https://doi.org/10.1139/e17-076, 1997.

Burn, C. R. and Kokelj, S. V.: The environment and permafrost of the Mackenzie Delta area, Permafrost Periglac., 20, 83–105, https://doi.org/10.1002/ppp.655, 2009.

Bull, W. B.: Geomorphology of segmented alluvial fans in western Fresno County, California. US Government Printing Office, USGS Prof Paper 352E, https://doi.org/10.3133/pp352E, 1964.

Carson, M.A. and Kirkby, M. J.: Hillslope Form and Process. Cambridge University Press, New York. 476 pp, https://doi.org/10.1017/S0016756800000546, 1972.

Chin, K. S., Lento, J., Culp, J. M., Lacelle, D., and Kokelj, S. V.: Permafrost thaw and intense thermokarst activity decreases abundance of stream benthic macroinvertebrates. Glob. Change Biol., 22, 2715–2728. https://doi.org/10.1111/gcb.13225, 2016.

Chipman, M. L., Kling, G. W., Lundstrom, C. C., and Hu, F. S.: Multiple thermo-erosional episodes during the past six millennia: Implications for the response of Arctic permafrost to climate change. Geology, 44, 439–442. https://doi.org/10.1130/G37693.1, 2016.

Church, M. and Slaymaker, O.: Disequilibrium of Holocene sediment yield in glaciated British Columbia. Nature. 337, 452–454. https://doi.org/10.1038/337452a0, 1989.

Dyke, A. S. and Prest, V. K.: Late Wisconsinan and Holocene History of the Laurentide Ice Sheet. Géographie Physique et Quaternaire, 41, 237-263. https//:doi.org/10.7202/032681ar, 1987.

Dyke, A. S., Moore, A., and Robertson, L.: Deglaciation of North America, Geological Survey of Canada, Ottawa, ON, Canada, Open File 1574, 2003.

Fulton, R. J. (compiler): Surficial Materials of Canada—Map 1880A Government of Canada, Natural Resources Canada, Geological Survey of Canada, Terrain Sciences Division Scale, 1: 5000000, https://doi.org/10.4095/205040, 1995.

Gould, S. B., Glenn, N. F., Sankey, T. T., and McNamara, J. P.: Influence of a Dense, Low-height Shrub Species on the Accuracy of a Lidar-derived DEM. Photogrammetric Engineering & Remote Sensing, 5, 421-431. https://doi.org/10.14358/PERS.79.5.421, 2013.

Holland, K. M., Porter, T. J., Froese, D. G., Kokelj, S. V., and Buchanan, C.: Ice-wedge evidence of Holocene winter warming in the Canadian Arctic. Geophys. Res. Lett., https://.doi.org/10.1029/2020GL087942, 2020.

Holloway, J. E., Lewkowicz, A. G., Douglas, T. A., Li, X., Turetsky, M. R., Baltzer, J. L., and Jin, H.: Impact of wildfire on permafrost landscapes: A review of recent advances and future prospects. Permafrost Periglac., https://doi.org/10.1002/ppp.2048, 2020.

Hornby, D. D.: RivEX (Version 10.25) [Software]. Available from http://www.rivex.co.uk. 2017.

Houben, A. J., French, T. D., Kokelj, S. V., Wang, X., Smol, J. P., and Blais, J. M.: The impacts of permafrost thaw slump events on limnological variables in upland tundra lakes, Mackenzie Delta region. Fundam. Appl. Limnol., 189(1), 11-35, https://doi.org/10.1127/fal/2016/0921, 2016.

Howard, A. D.: A detachment-limited model of drainage basin evolution. Water Resources Research, 30(7), 2261-2285, https://doi.org/10.1029/94WR00757, 1994.

Klar, A. Aharonov, E. Kalderon-Asael, B., and Katz, O.: Analytical and observational relations between landslide volume and surface area. J. Geophys. Res., 116, F02001, https://doi.org/10.1029/2009JF001604, 2011.

Kokelj, S. V. and Lewkowicz, A. G., 1999. Salinization of permafrost terrain due to natural geomorphic disturbance, Fosheim Peninsula, Ellesmere Island, 52(4), 372-385, http://doi.org/10.14430/arctic942, 1999.

Kokelj, S. V. and Jorgenson, M. T.: Advances in Thermokarst Research. Permafrost and Periglac., 24, 108–119, https://doi.org/10.1002/ppp.1779, 2013.

Kokelj, S. V., Zajdlik, B., and Thompson, M. S.: The impacts of thawing permafrost on the chemistry of lakes across the subarctic boreal tundra transition, Mackenzie Delta region, Canada. Permafrost and Periglac., 20, 185–199, https://doi.org/10.1002/ppp.641, 2009.

Kokelj, S. V., Lacelle, D., Lantz, T. C., Tunnicliffe, J., Malone, L., Clark, I. D., and Chin, K. S.: Thawing of massive ground ice in mega slumps drives increases in stream sediment and solute flux across a range of watershed scales. J. Geophys. Res.-Earth. 118, 681–692, https://doi.org/10.1002/jgrf.20063, 2013.

Kokelj, S. V., Tunnicliffe, J., Lacelle, D., Lantz, T. C., Chin, K. S., and Fraser, R.: Increased precipitation drives mega slump development and destabilization of ice-rich permafrost terrain, northwestern Canada, Glob. Planet. Change, 129, 56-68, https://doi.org/10.1016/j.gloplacha.2015.02.008, 2015.

Kokelj, S. V., Lantz, T. C., Tunnicliffe, J., Segal, R., and Lacelle, D.: Climate-driven thaw of permafrost preserved glacial landscapes, northwestern Canada. Geology, 45, 371–374, https://doi.org/10.1130/G38626.1, 2017a.

Kokelj, S. V., Tunnicliffe, J. F., and Lacelle, D.: The Peel Plateau of Northwestern Canada: An Ice-Rich Hummocky Moraine Landscape in Transition, in: Landscapes and Landforms of Western Canada, edited by: Slaymaker, O., Springer International Publishing, 109–122, http://link.springer.com/10.1007/978-3-319-44595-3_7, 2017b.

Kokelj, S. V, Palmer, M. J., Lantz, T. C., and Burn, C. R.: Ground Temperatures and Permafrost Warming from Forest to Tundra, Tuktoyaktuk Coastlands and Anderson Plain, NWT, Canada. Permafrost Periglac. 28, 543–551, https://doi.org/10.1002/ppp.1934, 2017c.

Kokoszka, J. and Kokelj, S. V.: 2020. Broad-scale mapping of hydrological features affected by slope-thermokarst from arctic drainage, Northwestern Canada: Methods and Data. Northwest Territories Geological Survey, NTGS Open Report, 2020-013, In revision 2020.

Lacelle, D., Bjornson, J., and Lauriol, B.: Climatic and geomorphic factors affecting contemporary (1950–2004) activity of retrogressive thaw slumps on the Aklavik Plateau, Richardson Mountains, NWT, Canada. Permafrost Periglac., 21, 1–15, https://doi.org/10.1002/ppp.666, 2010.

Lacelle, D., Brooker, A., Fraser, R. H., and Kokelj, S. V.: Geomorphology Distribution and growth of thaw slumps in the Richardson Mountains – Peel Plateau region, northwestern Canada. Geomorphology, 235, 40–51, https://doi.org/10.1016/j.geomorph.2015.01.024, 2015.

Lacelle, D., Fontaine, M., Pellerin, A., Kokelj, S. V., and Clark, I. D.: Legacy of Holocene Landscape Changes on Soil Biogeochemistry: A Perspective From Paleo-Active Layers in Northwestern Canada. J. Geophys. Res.- Biogeo., 124, 2662-2679, https://doi.org/10.1029/2018JG004916, 2019.

Lakeman, T. R. and England, J. H.: Paleoglaciological insights from the age and morphology of the Jesse moraine belt, western Canadian Arctic. Quaternary Sci. Rev., 47, 82–100, https://doi.org/10.1016/j.quascirev.2012.04.018, 2012.

Lantz, T. C. and Kokelj, S. V.: Increasing rates of retrogressive thaw slump activity in the Mackenzie Delta region, N.W.T., Canada, Geophys. Res. Lett., 35, L06502, https://doi.org/10.1029/2007GL032433, 2008.

Lantz, T. C., Gergel, S. E., and Kokelj, S. V.: Spatial heterogeneity in the shrub tundra ecotone in the Mackenzie Delta region, Northwest Territories: Implications for Arctic environmental change, Ecosystems, 13: 194–204, https://doi.org/ 10.1007/s10021-09-9310-0, 2010.

Levenstein, B., Culp, J. M., and Lento, J.: Sediment inputs from retrogressive thaw slumps drive algal biomass accumulation but not decomposition in Arctic streams, NWT, Freshw. Biol., 63, 1300–15, https://doi.org/10.1111/fwb.13158, 2018.

Lewkowicz, A. G. and Way, R. G.: Extremes of summer climate trigger thousands of thermokarst landslides in a High Arctic environment. Nat. Commun., 10, 1329, https://doi.org/10.1038/s41467-019-09314-7, 2019.

Littlefair, C. A., Tank, S. E., and Kokelj, S. V.: Retrogressive thaw slumps temper dissolved organic carbon delivery to streams of the Peel Plateau, NWT, Canada. Biogeosciences, 14, 5487–5505, https://doi.org/10.5194/bg-14-5487-2017, 2017.

Mackay, J. R.: The origin of massive icy beds in permafrost, western Arctic coast, Canada, Can. J. Earth Sci., 8, 397–422, https://doi.org/10.1139/e71-043, 1971.

Mann, D., Groves, H. P., Reanier, R. E., and Kunz, M. L.: Floodplains, permafrost, cottonwood trees and peat: What happened the last time climate warmed suddenly in arctic Alaska? Quat. Sci. Rev. 29, 3812–3830, https://doi.org/10.1016/j.quascirev.2010.09.002, 2010.

Malone, L., Lacelle, D., Kokelj, S., and Clark, I. D.: Impacts of hillslope thaw slumps on the geochemistry of permafrost catchments (Stony Creek watershed, NWT, Canada), Chem Geol., 356, 38–49, https://doi.org/10.1016/j.chemgeo.2013.07.010, 2013.

Meng, X., Currit, N., and Zhao, K.: Ground Filtering Algorithms for Airborne LiDAR Data: A Review of Critical Issues. Remote Sens., 2(3), 833-860, https://doi.org/10.3390/rs2030833, 2010.

Murton, J.: Thermokarst sediments and sedimentary structures, Tuktoyaktuk Coastlands, western Arctic Canada, Glob. Planet. Change, 28, 175–192, https://doi.org/10.1016/S0921-8181(00)00072-2, 2001.

Murton, J. B., Whiteman, C. A., Waller, R. I., Pollard, W. H., Clark, I. D., and Dallimore, S. R.: Basal ice facies and supraglacial melt-out till of the Laurentide Ice Sheet, Tuktoyaktuk Coast- lands, western Arctic Canada, Quat. Sci. Rev., 24, 681–708, https://doi.org/10.1016/j.quascirev.2004.06.008, 2005.

Natural Resources Canada.: Canada digital elevation data [dataset]. Ottawa, ON, Canada, https://open.canada.ca/data/en/dataset/7f245e4d-76c2-4caa-951a-45d1d2051333, 2015.

Natural Resources Canada.: National Hydro Network – NHN – GeoBase Series [dataset], Ottawa, ON, Canada https://open.canada.ca/data/en/dataset/a4b190fe-e090-4e6d-881e-b87956c07977, 2016.

Nitze, I., Grosse, G., Jones, B. M., Romanovsky, V. E., and Boike, J.: Remote sensing quantifies widespread abundance of permafrost region disturbances across the Arctic and Subarctic, Nat. Commun., 9, 5423, https://doi.org/10.1038/s41467-018-07663-3, 2018.

Northwest Territories Centre for Geomatics.: Northwest Territories SPOT Mosaic [dataset] http://www.geomatics.gov.nt.ca/dldsoptions.aspx, 2013.

Olefeldt, D., Goswami, S., Grosse, G., Hayes, D., Hugelius, G., Kuhry, P., McGuire, A. D., Romanovsky, V. E., Sannel, A. B. K., Schuur, E. A. G., and Turetsky, M. R.: Circumpolar distribution and carbon storage of thermokarst landscapes, Nat. Commun., 7, 13043, https://doi.org/10.1038/ncomms13043, 2016.

O'Neill, H. B., Burn, C. R., Kokelj, S. V., and Lantz, T. C.: "Warm" tundra: Atmospheric and near-surface ground temperature inversions across an alpine treeline in continuous permafrost, western Arctic, Canada, Permafrost Periglac., 26, 103– 118, https://doi.org/10.1002/ppp.1838, 2015.

O'Neill, H. B., Wolfe, S. A., and Duchesne, C.: New ground ice maps for Canada using a paleogeographic modelling approach, The Cryosphere, 13, 753-773, https://doi.org/10.5194/tc-13-753-2019, 2019.

Pollard, W. H.: Distribution and characterization of ground ice on Fosheim Peninsula, Ellesmere Island, Nunavut, in: Environmental response to climate change in the Canadian High Arctic, edited by: Garneau, M. and Alt, B. T., Geological Survey of Canada, Ottawa, ON, Canada, Bulletin 529, 207–233, 2000.

Porter, T. J., Schoenemann, S. W., Davies, L. J., Steig, E. J., Bandara, S., and Froese, D. G.: Recent summer warming in northwestern Canada exceeds the Holocene thermal maximum, Nat. Commun., 10:1631, https://doi.org/10.1038/s41467-019-09622-y, 2019.

Rampton, V. N.: Quaternary Geology of the Tuktoyaktuk Coastlands, Northwest Territories, Geological Survey of Canada, Ottawa, ON, Canada, Memoir 423, 1988.

Ramage, J. L., Irrgang, A. M., Herzschuh, U., Morgenstern, A., Couture, N., and Lantuit, H.: Terrain controls on the occurrence of coastal retrogressive thaw slumps along the Yukon coast, Canada. J. Geophys. Res.-Earth, 122, 1619–1634, https://doi.org/10.1002/2017JF004231, 2017.

Ramage, J. L., Irrgang, A. M., Morgenstern, A., and Lantuit, H.: Increasing coastal slump activity impacts the release of sediment and organic carbon into the Arctic Ocean, Biogeosciences, 15, 1483–1495, https://doi.org/10.5194/bg-15-1483-2018, 2018.

R Core Team. 2017. *R: A language and environment for statistical computing* (version 3.4.1). Vienna, Austria: R Foundation for Statistical Computing. http://www.R-project.org.

Rudy, A.C.A., and Kokelj, S.V., 2020. Inventory of retrogressive thaw slumps in the Willow River watershed, mapped using 1986, 2002, and 2018 Landsat imagery; Northwest Territories Geological Survey, NWT Open Report 2020-011, 4 pages and digital data.

Rudy, A. C. A., Lamoureux, S. F., Kokelj, S. V., Smith, I. R., and England, J. H.: Accelerating Thermokarst Transforms Ice-Cored Terrain Triggering a Downstream Cascade to the Ocean, Geophys. Res. Lett., 44, 11080–11087, https://doi.org/10.1002/2017GL074912, 2017a.

Rudy, A. C. A., Lamoureux, S. F., Treitz, P., Ewijk, K. V., Bonnaventure, P. P., and Budkewitsch, P.: Terrain Controls and Landscape-Scale Susceptibility Modelling of Active-Layer Detachments, Sabine Peninsula, Melville Island, Nunavut, Permafrost Periglac., 28(1), 79–91, https://doi.org/10.1002/ppp.1900, 2017b.

Rudy, A.C.A., Kokelj, S.V., and Kokozska, J., 2020. Inventory of retrogressive thaw slumps on the Peel Plateau and on southeastern Banks Island, Northwest Territories using 2017 Sentinel imagery; Northwest Territories Geological Survey, NWT Open Report 2020-012, 5 pages and digital data.

Segal, R. A., Lantz, T. C., and Kokelj, S. V.: Acceleration of thaw slump activity in glaciated landscapes of the Western Canadian Arctic, Environ. Res. Lett., 11(3), 034025, https://doi.org/10.1088/1748-9326/11/3/034025, 2016a.

Segal, R.A., Kokelj, S.V., Lantz, T.C., Durkee, K., Gervais, S., Mahon, E., Snijders, M., Buysse, J., and Schwarz, S.: Broad-scale mapping of terrain impacted by retrogressive thaw slumping in Northwestern Canada. Northwest Territories Geological Survey, NWT Open Rep. 2016-008, 17 pp., 2016b.

Segal, R.A., Lantz, T.C., and Kokelj, S.V.: Inventory of active retrogressive thaw slumps on eastern Banks Island, Northwest Territories. Northwest Territories Geological Survey, NWT Open Rep., 2015-021, 8 pp., 2016c.

Segal, R.A., Lantz, T.C., and Kokelj, S.V.: Inventory of active retrogressive thaw slumps in the Peel Plateau, Northwest Territories. Northwest Territories Geological Survey, NWT Open Rep.. 2015-020, 8 pp, 2016d.

Shakil, S., Tank, S.E., Kokelj, S.V., Vonk, J.E., and Zolkos, S.: Particulate dominance of organic carbon mobilization from thaw slumps on the Peel Plateau, NT: Quantification and implications for stream systems and permafrost carbon release. Environ. Res. Lett., Accepted 2020a.

Shakil, S., Zolkos, S., Chin, K., and Tank, S.: Total suspended solids data from streams draining permafrost thaw slumps on the Peel Plateau, Northwest Territories. Waterloo, Canada: Canadian Cryospheric Information Network (CCIN). https://doi.org/10.21963/13181, 2020b.

Smith, S. L., Romanovsky, V. E., Lewkowicz, A. G., Burn, C. R., Allard, M., Clow, G. D., Yoshikawa, K., and Throop, J.: Thermal state of permafrost in North America: a contribution to the international polar year, Permafrost Periglac., 21, 117–135, https://doi.org/10.1002/ppp.690, 2010.

Smith, M. W., Carrivick, J. L., and Quincey, D. J.: Structure from motion photogrammetry in physical geography. Prog. Phys. Geogr. Earth Environ., 40, 247–275, https://doi.org/10.1177/0309133315615805, 2016.

St. Pierre, K. A., Zolkos, S., Shakil, S., Tank, S. E., St. Louis, V. L., and Kokelj, S. V.: Unprecedented increases in total and methyl mercury concentrations downstream of retrogressive thaw slumps in the western Canadian Arctic. Environmental Science & Technology, 52(24), 14099-14109, https://doi.org/10.1021/acs.est.8b05348, 2018.

Tarboton, D., G.: A new method for the determination of flow directions and contributing areas in grid digital elevation models: Water Res. Res., 33, 309–319, https://doi.org/10.1029/96WR03137, 1997.

Tank, S. E., Striegl, R. G., McClelland, J. W., and Kokelj, S. V.: Multi-decadal increases in dissolved organic carbon and alkalinity flux from the Mackenzie drainage basin to the Arctic Ocean, Environ. Res. Lett., 11(5), 054015, https://doi.org/10.1088/1748-9326/11/5/054015, 2016.

Tank, S. E., Vonk, J. E., Walvoord, M. A., McClelland, J. W., Laurion, I., and Abbott, B. W.: Landscape matters: Predicting the biogeochemical effects of permafrost thaw on aquatic networks with a state factor approach. Permafrost Periglac., https://doi.org/10.1002/ppp.2057, 2020.

Turetsky et al.,: Carbon release through abrupt permafrost thaw. Nature Geoscience. https://doi.org/10.1038/s41561-019-0526-0, 2020.

Thienpont, J. R., Rühland, K. M., Pisaric, M. F. J., Kokelj, S. V., Kimpe, L. E., Blais, J. M., and Smol, J. P.: Biological responses to permafrost thaw slumping in Canadian Arctic lakes. Freshwater Biology, 58 (2), 337– 353, https://doi.org/10.1111/Fwb.12061, 2013.

van der Sluijs, J., Kokelj, S., Fraser, R., Tunnicliffe, J., and Lacelle, D.: Permafrost Terrain Dynamics and Infrastructure Impacts Revealed by UAV Photogrammetry and Thermal Imaging. Remote Sens., 10, 1734, https://doi.org/10.3390/rs10111734, 2018.

Vonk, J. E., Tank, S. E., and Walvoord, M. A.: Integrating hydrology and biogeochemistry across frozen landscapes, Nat. Commun., 10:5377, https://doi.org/10.1038/s41467-019-13361, 2019.

Walvoord, M. A. and Kurylyk, B. L.: Hydrological impacts of thawing permafrost-A review. Vadose Zone Journal, 15(6), https://doi:10.2136/vzj2016.01.0010, 2016.

Ward-Jones, M. K. W., Pollard, W. H., and Jones, B. M.: Rapid initialization of retrogressive thaw slumps in the Canadian high Arctic and their response to climate and terrain factors. Environment Research Letters. 14, 055006. https://doi.org/10.1088/1748-9326/ab12fd, 2019.

West, J. J. and Plug, L. J.: Time-dependent morphology of thaw lakes and taliks in deep and shallow ground ice. J. Geophys. Res. – Earth. 113: F01009, https.//doi.org/10.1029/2006JF000696, 2008.

Wohl., E: Connectivity in rivers. Prog. Phys. Geog., 41(3), 345-362, https://doi.org/10.1177/0309133317714972, 2017.

Young, J. M., van der Sluijs, J., Kokelj, S.V., and Froese, D.: Recent development of deep permafrost landslides (molard-type) in discontinuous permafrost from the central Mackenzie Mountain foothills, Northwest Territories, Canada. GSA Online, 26-30 October 2020.

Zolkos, S., Tank, S. E., and Kokelj, S. V.: Mineral Weathering and the Permafrost Carbon-Climate Feedback, Geophys. Res. Lett., 45, https://doi.org/10.1029/2018GL078748, 2018.

Zolkos, S., Tank, S. E., Striegl, R. G., Kokelj, S. V., Kokoszka, J., Estop-Aragones, C., and Olefeldt, D.: Thermokarst amplifies fluvial inorganic carbon cycling and export across watershed scales on the Peel Plateau, Canada. Biogeosciences, DOI: 10.5194/ https://doi.org/10.5194/ bg-17-5163--2020, 2020.

Zwieback, S., Kokelj, S. V., Gunther, F, Boike, J., Grosse, G., and Hajnsek, I.: Sub-seasonal thaw slump mass wasting in not consistently energy limited at the landscape scale. The Cryosphere, 12, 549–564, https://doi.org/10.5194/tc-12-549-2018, 2018.

1195

tc-2020-218 Supplementary Materials

Thaw-driven mass wasting couples slopes with downstream systems and effects propagate through Arctic drainage networks.

Steven V. Kokelj[1], Justin Kokoszka[1,2], Jurjen van der Sluijs[3], Ashley C.A. Rudy[1], Jon Tunnicliffe[4], Sarah Shakil[5], Suzanne E. Tank[5], Scott Zolkos[5,6]

[1]Northwest Territories Geological Survey, Yellowknife, NT, X1A 2L9, Canada

[2]Wilfrid Laurier University, Yellowknife, NT, X1A 2L9, Canada

[3]Northwest Territories Centre for Geomatics, Yellowknife, NT, X1A 2L9, Canada

[4]School of Environment, University of Auckland, Auckland, NZ

[5]Department of Biological Sciences, University of Alberta, Edmonton, AB, T6G 2E3, Canada

[6]Woodwell Climate Research Centre, Falmouth, MA, 02540, USA

Correspondence to: Steven V. Kokelj (steve_kokelj@gov.nt.ca)

Supplementary Materials include:

Supplementary Methods 1-3 (Geoprocessing steps for hydrological network analysis of slump effects and flow accumulation analysis).

Supplementary Figures 1-4.

Supplementary Tables 1-5.

Supplementary Videos 1-3. (URL links provided to SV 1 and 2. Video 3 is attached).

Supplementary Methods 1-3

Supplementary Method 1. Workflow for Willow River downstream accumulation of effects.

To quantify the scar and debris tongue areas of slope thermokarst features (STKs) affecting streams in the Willow River catchment and the downstream accumulation of STK scar areas through the fluvial network as an index for sedimentary and geochemical impact (main text Sect. 2.5.), we used delineations of STK scar/debris areas (Rudy and Kokelj, 2020), hydrologic data (streams and lakes) from the 1:50,000 National Hydro Network (NHN) dataset (Natural Resources Canada, 2016), and RivEX 10.25 software (Hornby, 2017). Data were compiled in ArcMap 10.6 and projected in the Canada Lambert Conformal Conic (CLCC) projected coordinate system. The workflow is documented in the following steps:

1) Manually delineated the Willow River catchment, in ArcMap 10.6, using topographic data from the 1:50,000 Canadian Digital Elevation Model (CDED) dataset (Natural Resources Canada, 2015). In order to aid the interpretation of the watershed boundary, NHN Primary Directed Network Linear Flow (PDNLF) and Waterbody Shapefiles (10MC002) were added to represent streams and lakes, respectively.
2) Clipped PDNLF and Waterbody feature classes (10MC002) to the Willow River catchment delineation from step 1.
3) Manually adjusted the PDNLF features to accommodate a recent channel abandonment and alteration in the routing of stream flow in the lower part of the catchment (main text Sect. 2.5.). Adjustments included:
    a) Removed PDNLF polyline (nid: 186964fe0c0c425c82150c486f7cbb71).
    b) Split PDNLF polyline (nid: a44c53c852f14ff29561a048435aca29).
    c) Added PDNLF polylines and assigned nid's: a1, a2, and a3.
    d) Reversed the direction of PDNLF polylines with the following nids:
        i) 8e0462e45626485bb69e6a7932f30c32
        ii) 9cb7a1ca015543a5ab825684402188b0
        iii) 6897bbd8a58c468c8cd15caf0610f5c2
        iv) D94bcd35f20d46f39d9f920b5e4e5365
        v) 92b84230ed9a4f6e9a881a18effa8884
        vi) f53ff86131864f3ea2adcfc8dd34b780
4) Constructed a topological network and ran 'Quality Control' tools using RivEX. Adjusted PDNLF polylines as necessary to ensure network continuity (i.e. consistent from- and to-nodes).
5) NHN PDNLF features represent the primary or (main route) of a stream. However, the PDNLF features are segmented in sections of braided channels that result in pseudo-nodes. To remove pseudo-nodes in sections of braided channels, a pseudo-node free network was generated using the ‘Create Network Free of Pseudo Nodes’ tool in RivEX.
6) Generated points at the intersections of streams and lakes and split the streams at the intersection points using a search radius of 5m.

7) Using the pseudo-node free network from step 6, constructed a topological network, using RivEx, and ran 'Quality Control' tools (except monotonic trends). During construction of the topological network, RivEX assigned each PDNLF polyline (segment) a unique ID (RivID).

8) Added a field (RivID) to the STK scar and debris shapefiles, from Rudy and Kokelj (2020), with the field type assigned as 'short integer'.

9) Assessed STK affects to stream and lake features, using delineations of STK scar and debris areas derived from 2018 Landsat imagery. STK features were interpreted to affect streams or lakes based on direct contact with the hydrological feature or based on the direction of down-slope flow indicated by topographic data (i.e. CDED). PDNLF segments affected by STK were recorded by assigning the value of the 'RivID' field, from the PDNLF segment, to the corresponding STK polygon. Special considerations included:

   a) Where STK(s) affected a lake, the RivID that corresponded with the hydrological/stream segment, located within the lake and at the lake outflow, was assigned to the STK polygon.

   b) In cases where STK affected multiple stream segments, the RivID from the most upstream segment, was assigned to the STK polygon. Some exceptions included:

      i) Where STK affected both a main-stem and a tributary the RivID from the stream segment with the largest contact length, with the STK polygon, was assigned to the STK polygon.

      ii) Where STK affected multiple headwater streams, the RivID from the stream segment with the largest contact length, with the STK polygon, was assigned to the STK polygon.

10) In order to ensure the consistency of areal measurements from the research paper, the area of delineations for scar and debris areas, using 2018 Landsat, were computed using the Universal Transverse Mercator Zone 8, North American Datum 1983 (NAD 83) coordinate system.

11) Using ArcMap's 'Summary Statistics' tool, a summary table was generated for the STK scar area shapefile, where the areas of all disturbed features were summed for each RivID value.

12) Repeated step 9 for the STK debris area shapefile.

13) Joined the summary tables, from step 9 and 10, to the stream network based on the RivID field.

14) Using RivEX, assigned Strahler Order to stream segments and performed upstream accumulations for both the scar and debris areas. For the abandoned channel, accumulation values were manually re-set to 0.

15) Using the 'Feature to Point' tool in ArcMap, generated points for each stream segment affected by STK.

16) Scar and debris areas were summarized by Strahler Order (excluding hydrological/stream segments within lakes.)

Supplementary Method 2. Workflow for broad-scale downstream accumulation of effects.

To quantify the number of hydrologic features (streams, lakes, and coastlines) affected by slope thermokarst features (STKs) and to propagate the downstream effects of STK (main text Sect. 2.5), within Arctic drainage from continuous permafrost, we used an inventory of hydrologic features affected by STK (Kokoszka and Kokelj, 2020), hydrologic data (streams, lakes and coastlines) from the 1:50,000 National Hydro Network (NHN) dataset (Natural Resources Canada, 2016), and RivEX 10.25 Software (Hornby, 2017). Data were compiled in ArcMap 10.6.

Due to the significant amount of hydrologic data required to propagate STK affects throughout the entire study basin, geoprocessing was completed on the basis of Water Survey of Canada sub-sub-drainage areas (NHN Work Unit), for a total of 68 Work Units. A complete list of NHN Work Units is available from Kokoszka and Kokelj, 2020. Because the fluvial network was connected across NHN Work Units, accumulation analyses were first conducted for Work Units located in the headwaters of the study basin. Accumulation analyses were then conducted within downstream NHN Work Units to ensure propagation of STK effects throughout the entire study basin. The workflow involved the following steps:

1) For a specified Work Unit, NHN Primary Directed Network Linear Flow (PDNLF), Waterbody, and Littoral feature classes were imported to ArcMap to represent streams, lakes, and coastlines, respectively.
2) Re-projected the PDNLF, Waterbody, and Littoral feature classes to the Canada Lambert Conformal Conic projected coordinate system (CLCC).
3) Removed features from the Waterbody feature class that were attributed as watercourses or intermittent.
4) Modifications to hydrologic data were made for the specified NHN Work Units:
    a) NHN Work Unit 10TB002: Removed a littoral segment that extended beyond the coastline into the Arctic Ocean (nid = 4bcd3316c65c449a99f307803d0bddb3).
    b) NHN Work Unit 10MD002: Clipped hydrologic data to the reduced extent of the Work Unit delineation (Kokoszka and Kokelj, 2020).
    c) NHN Work unit 10MC002: Re-routed the Mackenzie River to propagate STK effects through the eastern portion of the Mackenzie Delta as opposed to the central region of the Mackenzie Delta by adding a PDNLF polyline (nid = 10mc002ADD01) and removing a PDNLF polyline (nid = 874e0d518ce34245a367869ddcbadeab).
5) Joined the attribute tables from the PDNLF feature class and STKI_Stream feature class (Kokoszka and Kokelj, 2020) based on the 'nid' fields.
6) Added an attribute field (ValDirect) to the PDNLF feature class with the field type assigned as 'short integer'.
7) Selected PDNLF features where the 'STK' field was equal to 1 (directly affected by STK) and from the selected PDNLF features, attributed the 'ValDirect' field with a value of 1.
8) Constructed a topological network and ran 'Quality Control' tools using RivEX. Error logs were generated by RivEX and were inspected for quality control. For this project, the error logs generated by RivEX included:

a) Small polylines composed of two vertices: Small polylines (< 1m) in length. Small polylines do not affect the integrity of the topological network. As such, for the purpose of this project, small polylines were not adjusted during the quality control process.

b) Polyline spikes: A digitization error where a single vertex is out of place that creates an acute angle along the length of the polyline. Spikes do not affect the integrity of the topological network, but can increase the length of a polyline segment. For the purpose of this project, polyline spikes were not adjusted because the increase in polyline length was deemed negligible compared to the overall length of polylines within the study basin.

9) Computed the upstream accumulation of direct STK affects, within the NHN Work Unit. In RivEX, selected 'attribute network' -> 'accumulate attribute in network' -> 'Run Tool' -> selected the variable to accumulate as 'ValDirect' -> specified the output field as 'AccDirect' -> selected 'OK'.

10) Identified indirectly affected PDNLF polylines (segments) (i.e. segments located upstream of directly affected segments). In ArcMap, started an edit session -> from the 'selection' tab, selected 'select by attribute' -> set selection method as 'create new selection' -> from the PDNLF layer, selected features where the 'AccDirect' field was > 0 -> selected 'OK' -> attributed the selected features 'STK' field with a value of 2 (indirect).

11) Identified PDNLF segments that were directly and indirectly affected by STK. In ArcMap, started an edit session -> from the 'selection' tab, selected 'select by attribute' -> set the selection method as 'create new selection' -> from the PDNLF layer, selected features where the 'AccDirect' field was > 0 -> selected 'OK' -> started a new selection from the 'selection' tab by selecting 'select by attribute' -> set selection method as 'from the current selection' -> from the PDNLF layer, selected features where the 'STK' field was not 0 -> selected 'OK' -> attributed the selected features 'STK' field with a value of 3 (both).

12) In ArcMap, visually inspected the attribution of the "STK' field, for PDNLF segments, by adjusting the colour scheme of the 'STK' field as follows: 'STK' = 0 to Cretan Blue (no STK affect), 'STK' = 1 to Mars Red (direct STK affect), 'STK' = 2 to Electron Gold (indirect STK affect), and 'STK' = 3 to Tuscan Red (both).

13) Identified indirectly affected Waterbody features (i.e. located upstream of directly affected PDNLF segments). In ArcMap, started an edit session -> from the 'selection' tab, selected 'select by attribute' -> set the selection method as 'create new selection' -> from the PDNLF layer, selected features where the 'AccDirect' field was > 0 and the 'Pseudo' field was equal to 0 -> selected 'OK' -> started a new selection from the 'selection' tab by selecting 'select by location' -> set the selection method as 'select features from' -> set the target layer as the Waterbody layer -> set the source layer as the PDNLF layer and ensured the 'use selected features' radio button was checked -> set the selection method as 'contain the source layer' -> selected 'OK' -> attributed the selected features 'STK' field with a value of 2 (indirect).

14) Identified Waterbody features that were directly and indirectly affected by STK. In ArcMap, started an edit session -> from the 'selection' tab, selected 'select by attribute' -> set selection method as 'create new selection' -> from the

PDNLF layer, selected features where the 'AccDirect' field was > 0 and the 'Pseudo' field was equal to 1 -> started a new selection from the 'selection' tab by selecting 'select by location' -> set the selection method as 'select features from' -> set the target layer as the Waterbody layer -> set the source layer as the PDNLF layer and ensured the 'use selected features' radio button was checked -> set the selection method as 'contain the source layer' -> selected 'OK' -> attributed the selected features 'STK' field with a value of 3 (both).

15) In ArcMap, visually inspected the attribution of the "STK' field of Waterbody features by adjusting the colour scheme of the 'STK' field as follows: 'STK' = 0 to Cretan Blue (no STK affect), 'STK' = 1 to Mars Red (direct STK affect), 'STK' = 2 to Electron Gold (indirect STK affect), and 'STK' = 3 to Tuscan Red (both).

16) In ArcCatalog, generated a new point feature class (AccSink) and added an attribute field (ValDirect) with the field type assigned as 'short integer'.

17) Locations where stream and lake derived STK affects propagated to the coastline were identified by visually inspecting the downstream path of PDNLF segments based on the 'STK' field's colour scheme (i.e. PDNLF segments that were not Cretan Blue) and mapping AccSink points at the downstream end of PDNLF segments, that terminated at the coastline. In order to represent the number of upstream (accumulated) hydrologic features directly affected by STK at the coastline, the value of the 'AccDirect' field, from the PDNLF segment, was attributed to the 'AccDirect' field of the AccSink point.

18) Because PDNLF segments represent the main route of network flow, in some cases streams affected by STK did not propagate to the main stem of the Mackenzie River (NHN Work Unit: 10LC000). In such cases, the corresponding value of the 'AccDirect' field was added to the AccSink point at the outlet of the Mackenzie River main stem. Similarly, values of the 'AccDirect' fields, for streams located near the outer reach of the Mackenzie Delta, were consolidated to the AccSink point located at the outlet of the Mackenzie River main stem.

19) Generated a 500m buffer (AccSinkBuffer) around the AccSink points.

20) Identified indirectly affected Littoral features (i.e. features located downstream of directly and indirectly affected PDNLF segments). In ArcMap, started an edit session -> from the 'selection' tab, selected 'select by location' -> set the selection method as 'select features from' -> set the target layer as the Littoral layer -> set the source layer as the AccSinkBuffer layer -> set the selection method as 'intersect the source layer' -> selected 'OK' -> started a new selection from the 'selection' tab by selecting 'select by attribute' -> set the selection method as 'select from current selection' -> from the Littoral layer, selected features where the 'STK' field was equal to 0 -> selected 'OK' -> attributed the selected features 'STK' field with a value of 2 (indirect).

21) Identified Littoral features that were directly and indirectly affected by STK. In ArcMap, started an edit session -> from the 'selection' tab, selected 'select by location' -> set the selection method as 'select features from' -> set the target layer as the Littoral layer -> set the source layer as the AccSinkBuffer layer -> set the selection method as 'intersect the source layer' -> selected 'OK' -> started a new selection from the 'selection' tab by selecting 'select by attribute' -> set selection method as 'select from current selection' -> from the Littoral layer, selected features where

the 'STK' field was equal to 1 -> selected ‘OK’ -> attributed the selected features 'STK' field with a value of 3 (both).

22) Repeated steps 1 to 21 for each NHN Work Unit. Where STK affects propagated between NHN Work Units, prior to conducting the accumulation analysis the value of the 'AccDirect' field, for the upstream PDNLF segment (i.e. located in the upstream NHN Work Unit), was attributed to the 'AccDirect' field for the downstream PDNLF segment (i.e. located in the downstream NHN Work Unit).
23) For each NHN Work Unit, segments from the PDNLF feature class, where the 'STK' field was equal to 1 (i.e. directly affected by STK), were selected and exported as new feature classes. The feature classes were then merged to generate a downstream trace that represented the propagated and accumulated STK affects across the entire study basin.
24) The downstream trace was visually inspected to ensure continuity of STK affects between NHN Work Units.

Supplementary Method 3. RivEX Workflow to Assess Strahler Order

To derive the Strahler stream and lake orders within four watersheds (Keele/Redstone, Peel, Amundsen Gulf, and Banks Island) of the Arctic drainage area from continuous permafrost of northwestern Canada (main text Sect. 2.5), we used hydrologic data (streams and lakes) from the 1:50,000 National Hydro Network dataset (NHN) (Natural Resources Canada, 2016) and RivEX 10.25 Software (Hornby, 2017). Data were compiled in ArcMap 10.6. Steps in the workflow included:

1) In ArcMap, imported NHN Primary Directed Network Linear Flow (PDNLF), Waterbody, and NHN WorkUnit feature classes to represented streams, lakes, and hydrologic boundaries, respectively.
2) Generated watershed delineations by merging the following NHN Work Unit feature classes for each specified watershed:
    a) Keele/Redstone: 10HA000 and 10HB000
    b) Peel: 10MA000, 10MB000, and 10MC002
    c) Amundsen Gulf: 10OA001, 10OA002, 10OB000, 10OC001, and 10OC002
    d) Banks Island: 10TA001, 10TA002, 10TA003, 10TA004, 10TB001, and 10TB002
3) Modifications to hydrologic data were made for the specified NHN Work Units:
    a) NHN Work Unit 10TB002: Removed a littoral feature that extended beyond the coastline into the Arctic Ocean (nid = 4bcd3316c65c449a99f307803d0bddb3).
    b) NHN Work Unit 10MC002: Work Unit feature class was manually reduced to specify the drainage area from a specified segment of the Peel River (nid = f1d3cf54069c4e4f9f35ddef517e4b9d). The 10MC002 Work Unit area included PDNLF polylines within the Mackenzie Delta. Computing Strahler order for PDNLF polylines within the 10MC002 Work Unit would have required computing Strahler order for the entire Mackenzie River, which was not feasible given computational restraints.
4) Merged PDNLF and Waterbody feature classes for their respective watersheds (see step 2). The merged PDNLF and Waterbody feature classes, from the Peel watershed, were clipped to the reduced watershed delineation (see Step 3b).
5) Constructed a topological network for each watershed using the merged PDNLF feature classes (see Step 4), and ran ‘Quality Control’ tools, using RivEX. The quality control error logs included small polylines and spikes within the networks. However, the presence of small polylines and spikes do not affect the topology of the network and were disregarded in the quality control process.
6) Computed Strahler Order for PDNLF polylines by selecting 'Strahler' from the 'Network Attribution" tool in RivEX.
7) Performed a spatial join between PDNLF polylines (join features) and Waterbody polygons (target features) to determine lake order. The spatial join matched PDNLF polylines that were located within Waterbody features based on the maximum Strahler Order of the PDNLF polylines, using a one-to-one join operation.
8) Visually inspected the Strahler stream and lake order outputs for quality assurance.

Supplementary Figures 1-4

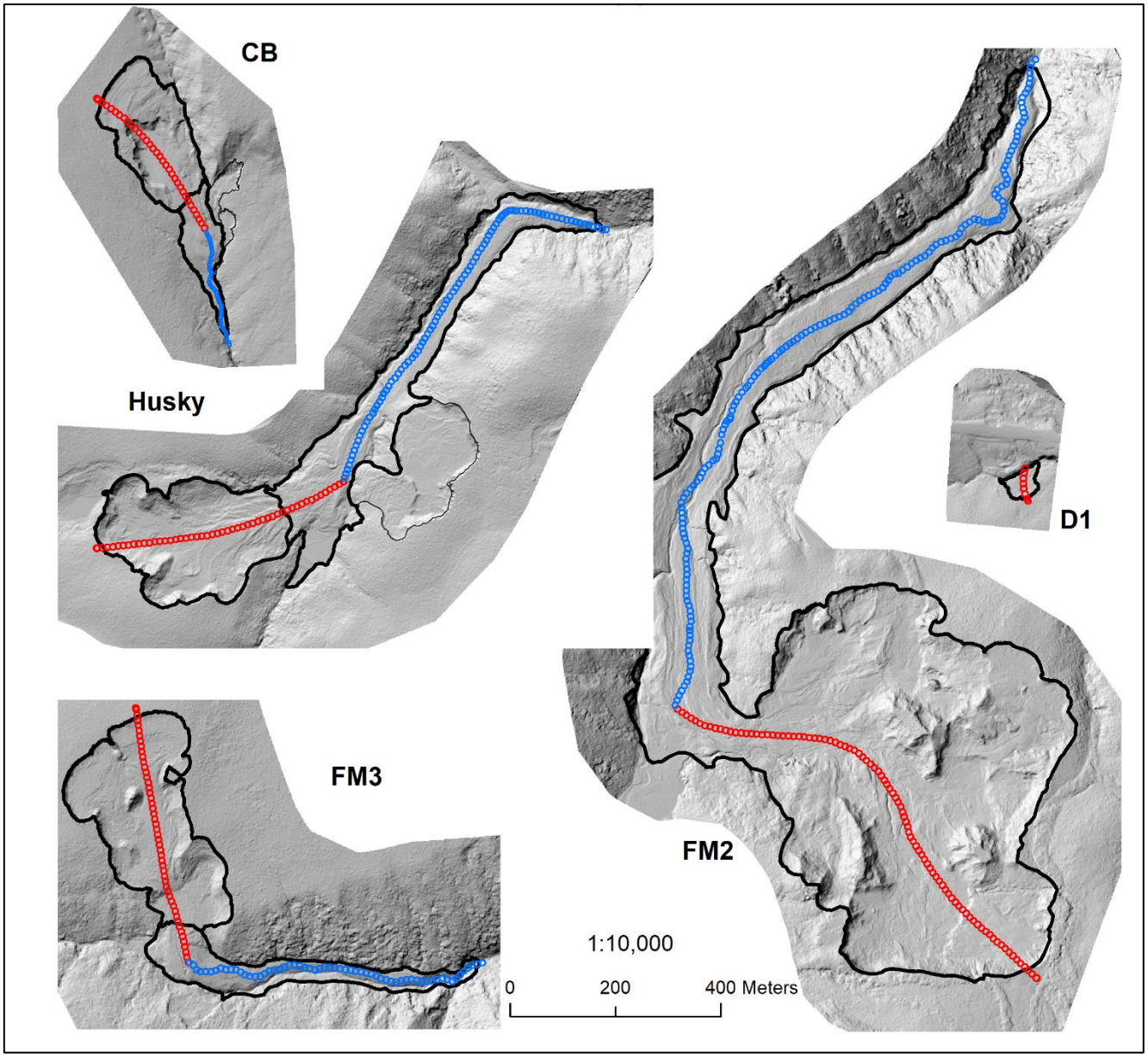

Figure S1. Retrogressive thaw slumps and debris tongues showing transects for the topographic profiles in Figure 2g. The terrain models are from UAV surveys described in Sect. 2.2, 2.3 and summarized in Table S2.

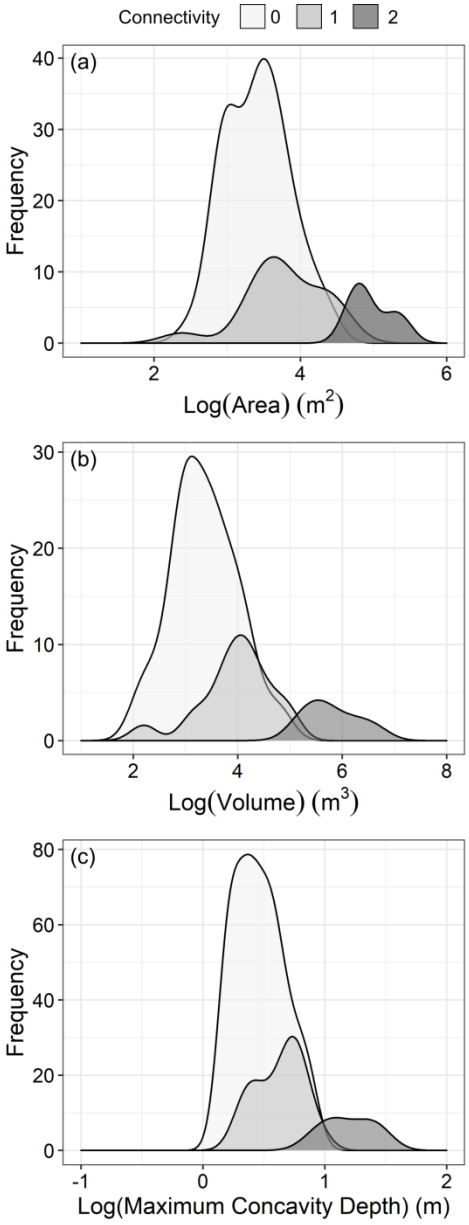

Figure S2. Frequency distributions for thaw slump (a) area, (b) volume and (c) maximum concavity depth grouped by downstream connectivity based on slump digitization of 2011 LiDAR. Class 0 indicates no physical connection between the slump and downstream environment; 1 is a physical connection between an active or bare scar and the downstream environment; and 2 is evidence of downstream deposition, which is expressed as a debris tongue in a valley bottom, or a sediment lobe protruding into an adjacent lake or coastline.

Figure S3. Willow River main stem view looking southwest. Photograph shows small shallow slides in foreground, and large deep-seated translational failures which have evolved into retrogressive thaw slumps. Slide materials have runout onto the braided floodplain. Numerous retrogressive thaw slumps are visible in background on slopes of incised tributary streams. Photograph is upstream view towards inset (b) on Figure 6.

Figure S4. Panels show downstream effects of slope thaw-driven mass wasting and some oblique photographs of slope disturbances. Examples of thaw-driven increases in downstream sedimentation include examples from: i. Sachs River inflow to Big Fish Lake, Banks Island; ii. Inflow of Miner and Kugalik Rivers to Husky Lake estuary, Mackenzie Delta region; iii. Development of massive, deep seated translational failure on Johnson River, central Mackenzie Valley. Supporting oblique photographs of thaw-driven sediment sources are provided for ii and iii. Locations of i, ii and iii are indicated on Figure 8.

i. Sachs River and Big Fish Lake, Banks Island (a) 1985 and (b) 2018 (Lat/long: 71.8237 N, -124.4983 W). (c) ~~is an~~ August 1, 2015 photograph of a large retrogressive thaw slump located on a Sachs River tributary about 35 km upstream of Big Fish Lake. (d) ~~is the~~ inflow of Sachs River into Big Fish Lake during summer baseflow conditions (August 1, 2015), showing slump derived turbidity.

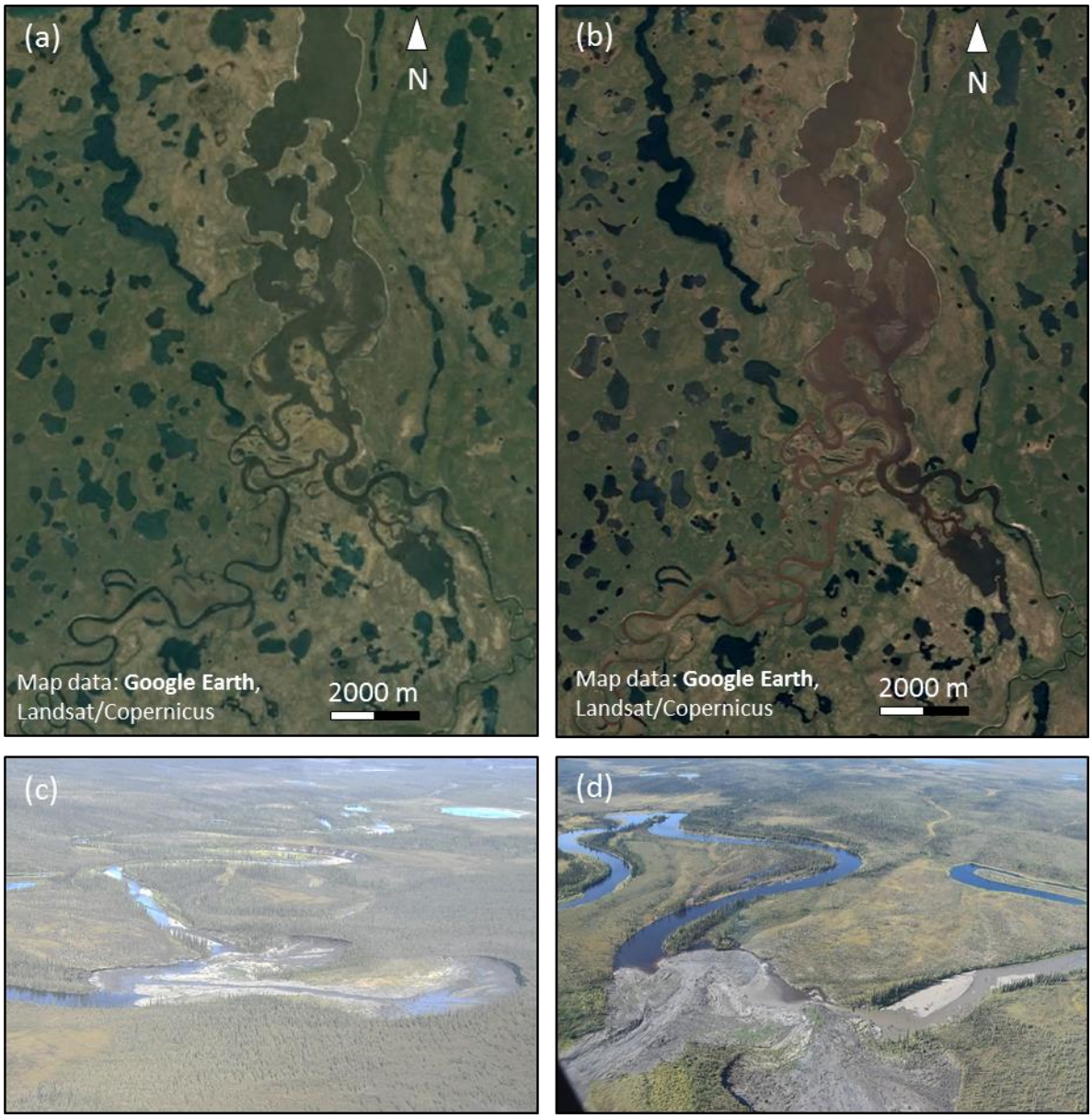

ii. Inflow of Miner River (lower left) and Kugalik River (lower right) into Husky Lake estuary (a) 1991 and (b) 2018. Note turbidity of Miner River and estuary in 2018 (Lat/long: 69.1617 N, -131.0135 W). (c) Large retrogressive thaw slumps on upper sections of Miner River and effects of thaw-driven slope to stream sediment delivery. (d) ~~shows dark,~~ DOC-rich water of undisturbed Miner River on left, and turbid conditions downstream (to the right) of the debris tongues which have blocked the channel. Photographs are from summer 2020.

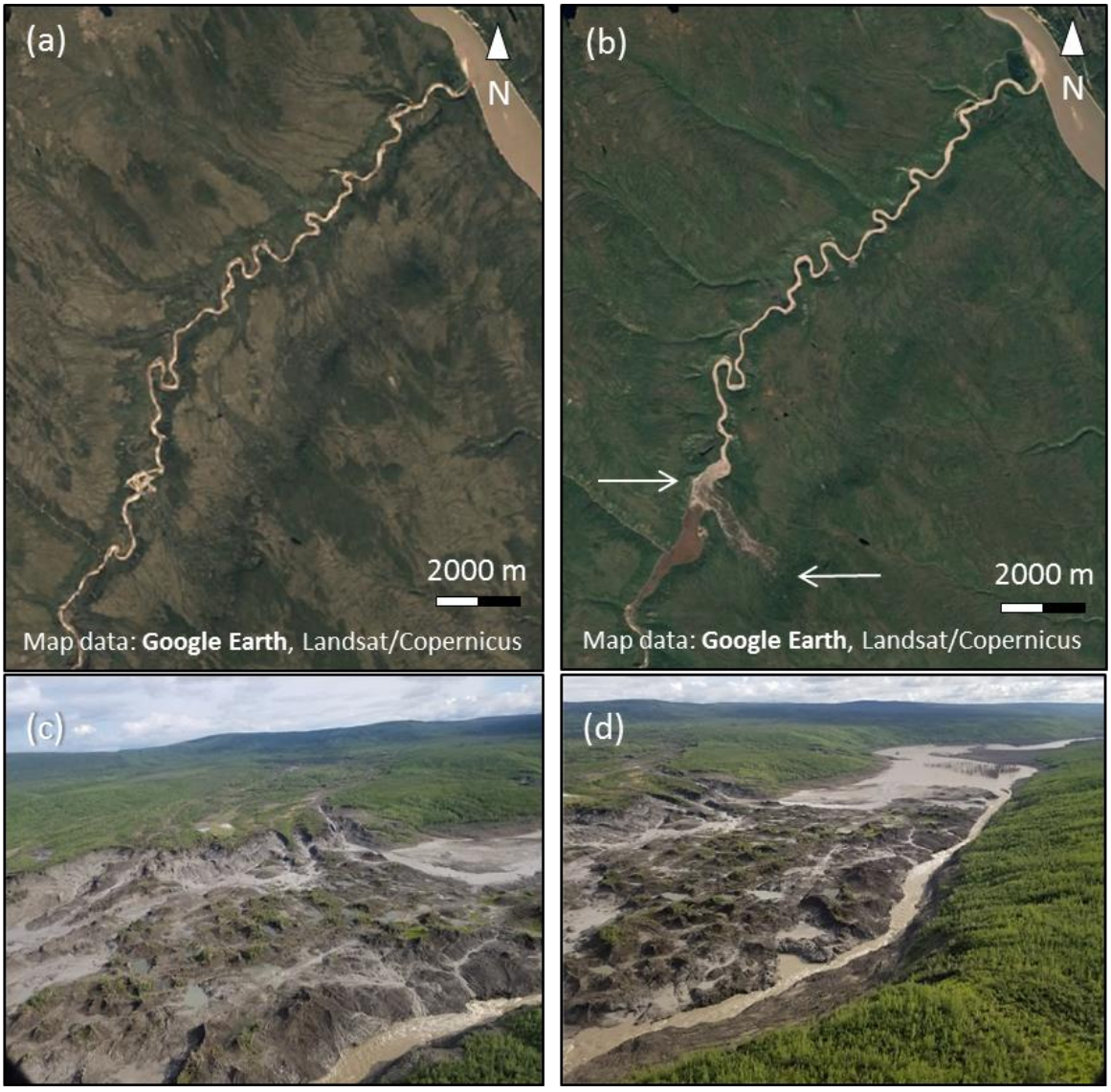

iii. Johnson River near the confluence with Mackenzie River showing changes caused by a major deep-seated translational failure that occurred in fall 2017. Images show the area in (a) 1991 and (b) following major slide development (2018) (Lat/long: 63.6587 N, -124.0530 W). Arrows on (b) are 2 km in length and show the upper part of the slide and the debris deposit. Note the high turbidity ~~in~~ the river downstream of the landslide and the development of an alluvial deposit at Johnson River confluence with the Mackenzie River in the upper right. (c, d) ~~are~~ southward oblique views showing the enormous debris flow deposit that has infilled the Johnson River valley. The fine-grained, ice-rich permafrost materials that have been translocated into the valley are melting out causing thermokarst and continued mobilization of materials. For scale, note forest cover on the blocks of permafrost debris that slid along a 3-5° slope into the valley. Blockage of Johnson River caused an upstream lake to form, and the river has incised a canyon through the debris deposit.

Supplementary Tables 1-5

Table S1. Summary of research ~~goals,~~ the spatial datasets and related methods sections, geographic locations, and sources of the datasets used in this multi-scale study.

Research ~~goal~~	Base datasets	Geographic locations (Figure 1)	Data source
(A) Thaw-driven geomorphic change and slope to stream connectivity	*Sect. 2.2 & 2.3*; 2011 LiDAR (1 m DEM)	Peel Plateau; Anderson Plain & Tuk Coastlands	NWT Centre for Geomatics, Gov. of Northwest Territories
	Sect. 2.2 & 2.3; UAV imagery (≤ 3 cm, downsampled to 1 m DEM) (Table S2)	Peel Plateau	van der Sluijs et al., 2018; NWT Centre for Geomatics, Gov. of Northwest Territories
(B) Medium scale catchment effects of thaw-driven mass wasting	*Sect. 2.4*; 2016-2017 Sentinel2 orthomosaic, 10m	Peel Plateau; SE Banks Island	Rudy et al., 2020
	Sect. 2.4; 1986, 2002, 2018 Landsat, 30 m	Willow River	Rudy and Kokelj, 2020
	Sect. 2.4; Stream sediment and discharge data, Peel watershed	Peel Plateau	Shakil et al., 2020b
(C) Distribution of mass-wasting effects on fluvial networks and propagation across Arctic drainage from continuous permafrost of Northwestern Canada	*Sect. 2.5*; SPOT 4/5 (2004-2010), 15m; Sentinel-2 (2016, 2017), 10m	Arctic drainage from continuous permafrost & Banks, Amundsen, Peel, Keele-Redstone watersheds	Kokoszka and Kokelj, 2020
	Sect. 2.5; National Hydro Network dataset		NRCan, 2016

Table S2. Summary of UAV surveys conducted over the four-year campaign to support Sect. 3.1-3.3 (modified from Van der Sluijs et al., 2018).

Site	Date	UAV	Res (cm)	Area (ha)	Photos (no.)
D1 (67.1771° N -135.7555° W)	2015-07-28	PX8	1.5	4.3	295
	2015-07-29	PX8	1.5	3.8	291
	2016-08-03	Inspire	1.3	1.7	79
	2017-07-27	P4P	1.2	6.3	316
	2018-09-18	eBee	1.5	9.0	311
FM3 (67.2539° N -135.2732° W)	2015-07-29	PX8	1.9	28.3	658
	2016-08-02	Inspire	2.4	34.3	583
	2017-07-26/28	eBee	3.3	365.0	3,499
	2018-09-19	eBee	3.3	88	463
FM2 (67.2545° N -135.2286° W)	2016-08-02	Inspire	2.4	83.6	1516
	2017-07-26/28	eBee	3.3	365.0	3499
	2018-09-18	eBee	3.3	161	982
Husky (67.5207 ° N -135.3005 W)	2016-08-03	Inspire	1.7	36.8	773
	2017-07-28	eBee	3.4	100.5	723
	2018-09-19	eBee	3.2	90.0	510
CB (67.1814° N -135.7295° W)	2015-07-28	PX8	1.5	12.1	711
	2018-09-18	eBee	2.7	28.1	438
Mean			2.3	83	920
Stdev			0.8	115	1024
Sum				1,053	15,647

Note: Flights conducted for thermal mapping, oblique still photography and video purposes are not included. Table headings "Res" is resolution or pixel size. UAV platforms: Spyder PX8 Plus (PX8), Phantom 2 Vision Plus (P2), RX4-S Surveyor (RX4), Inspire 1 Pro (Inspire), eBee Plus RTK/PPK (eBee), and Phantom 4 Pro (P4P).

Table S3 Summary statistics of slump area, volume and scar concavity depth estimates for the Peel Plateau, and Anderson Plain and Tuktoyaktuk Coastlands 2011 LiDAR Corridor (n=71).

		Area (m^2)	Volume (m^3)	Concavity depth (m)	
				Mean	**Maximum**
Mean		14,934	-106,003	-1.82	-4.76
Median		3,323	-3,860	-1.18	-3.36
Std. Deviation		38,056	480,480	2.27	4.73
Skewness		5	-6	-3.62	-3.34
Kurtosis		26	45	15.46	12.85
Minimum		242	-3,653,390	-14.39	-28.37
Maximum		253,937	-128	-0.11	-1.48
Sum		1,060,280	-7,526,216		
Percentiles	25	1,495	-13,982	-2.10	-5.47
	50	3,323	-3,860	-1.18	-3.36
	75	7,730	-995	-0.70	-2.22

Table S4. Summary statistics for size metrics of active thaw-slumps in the Willow River catchment for 1986, 2002 and 2018. Area estimates were determined by digitizing orthorectified, color balanced, ~~could~~-free Landsat imagery (Rudy and Kokelj, ~~2002~~). Thaw slump volume and maximum concavity depth were estimated using relationships shown in Figure 4.

Parameter	**1986**	**2002**	**2018**
Scar area (m^2)			
Count	21	73	198
Cumulative area	105,081	669,249	3,545,445
Median	4,512	5,688	8,293
Mean (STdev)	5,004 (2,601)	9,768 (10,608)	17,906 (29,685)
Max	13,497	63,838	198,986
Min	1,649	766	1,073
Scar volume (m^3)			
Cumulative volume	144,868	1,437,340	11,688,197
Median	5,537	7,687	13,119
Mean (STdev)	6,898 (5,513)	19,690 (35,515)	59,031 (161,741)
Max	26,154	236,479	1,184,216
Min	1,330	449	723
Concavity depth (m)			
Median	3.6	3.9	4.5
Mean (STdev)	3.6 (0.67)	4.1 (1.5)	5.1 (2.1)
Max	5.3	9.3	14.1
Min	2.5	1.9	2.1
Debris tongue area (m^2)			
Count	6	31	67
Median	5,046	6,165	8,884
Mean (STdev)	18,655 (24,511)	9,681 (10,071)	15,394 (18,857)
Max	59,011	39,682	100,569
Min	1,631	1,250	1,087

* Landsat dates: 1986-07-07; 2002-07-20; 2018-07-22

Table S5. Results Dunn's post-hoc test for comparison of thaw slump scar area between 1986, 2002 and 2018 following a Kruskal-Wallis Rank Sum test (p>0.00001).

Comparison dates	Z score	P. unadjusted	P. adjusted
2002-2018	-3.4614	0.0005	0.0008
1986-2002	1.4714	0.1411	0.1411
1986-2018	3.6529	0.0002	0.0008

***Dunn's post-hoc results indicate significant differences between 1986 and 2018, and 2002 and 2018.

~~Supplementary Videos 1-3~~

Video S1.
Video shows truncation of a small tundra lake by thaw-slump growth causing rapid drainage on the Peel Plateau in 2015 (67.5207 ° N -135.3005° W).
https://www.nwtgeoscience.ca/services/permafrost-thaw-slumps/video-permafrost-thaw-causes-lake-drainage-peel-plateau-nwt

Video S2.
UAV fly through of a large active retrogressive thaw slump in Willow River catchment shown in Figure 6b (68.1119° N -135.6806° W).
https://www.nwtgeoscience.ca/services/permafrost-thaw-slumps/drone-survey-permafrost-mega-slump-willow-river-nwt

Video S3.
Animated GIF image depicting a Landsat time-series animation covering the 1985-2019 period for lower Willow River catchment on the eastern edge of the Mackenzie Delta showing evolution of major thaw slumps most notably in lower left corner of imagery (see Fig. 6b). The time series shows acceleration of disturbance activity in the late 1990s and early 2000s, alluviation of the Willow River Channel and infilling of the large Mackenzie Delta lake from 2007 and 2019 with slump-derived sediment transported by the Willow River (Fig. 6c). Animation was generated using two ©Google Earth Engine applications: 1) the "LandTrendr time series animation app, URL: https://emaprlab.users.earthengine.app/view/lt-gee-time-series-animator" to generate the animation, and 2) the "Snazzy EE-TS-GIF, URL: https://jstnbraaten.shinyapps.io/snazzy-ee-ts-gif/" for annotations. The Landsat time series has been smoothed by LandTrendr spectral-temporal segmentation on ©Google Earth Engine (Kennedy et al., 2018). URL: https://emapr.github.io/LT-GEE/ui-applications.html (Accessed 3 August 2020).

References

Hornby, D. D.: RivEX (Version 10.25) [Software]. Available from http://www.rivex.co.uk. 2017.

Kennedy, R. E., Yang, Z., Gorelick, N., Braaten, J., Cavalcante, L., Cohen, W. B., and Healey, S.: Implementation of the LandTrendr Algorithm on Google Earth Engine. Remote Sens., 10, 691, https://doi.org/10.3390/rs10050691, 2018.

Kokoszka, J. and Kokelj, S. V.: 2020. Broad-scale mapping of hydrological features affected by slope-thermokarst from arctic drainage, Northwestern Canada: Methods and Data. Northwest Territories Geological Survey, NTGS Open Report, 2020-013, In revision 2020.

Natural Resources Canada.: National Hydro Network – NHN – GeoBase Series [dataset], Ottawa, ON, Canada https://open.canada.ca/data/en/dataset/a4b190fe-e090-4e6d-881e-b87956c07977, 2016.

Natural Resources Canada.: Canada digital elevation data [dataset]. Ottawa, ON, Canada, https://open.canada.ca/data/en/dataset/7f245e4d-76c2-4caa-951a-45d1d2051333, 2015.

Rudy, A.C.A., and Kokelj, S.V., 2020. Inventory of retrogressive thaw slumps in the Willow River watershed, mapped using 1986, 2002, and 2018 Landsat imagery; Northwest Territories Geological Survey, NWT Open Report 2020-011, 4 pages and digital data.

Rudy, A.C.A., Kokelj, S.V., and Kokozska, J., 2020. Inventory of retrogressive thaw slumps on the Peel Plateau and on southeastern Banks Island, Northwest Territories using 2017 Sentinel imagery; Northwest Territories Geological Survey, NWT Open Report 2020-012, 5 pages and digital data.